TECHNISCHE UNIVERSITÄT WIEN

DIPLOMARBEIT

Determination of the Cabibbo-Kobayashi-Maskawa matrix element $|V_{cb}|$ from inclusive observables in semileptonic B meson decays

ausgeführt an der
Fakultät für Physik der Technischen Universität Wien

in Zusammenarbeit mit dem
Institut für Hochernergyphysik der Österreichischen Akademie der Wissenschaften

zur Erlangung des akademischen Grades eines
Diplom-Ingenieurs

im Rahmen des Studiums
066 461 Technische Physik

unter der Anleitung von
Privatdoz. Dipl.-Ing. Dr.techn. Christoph Schwanda

eingereicht von

Felix Troneberger, BSc
Matr.Nr.: 11819539

February 12, 2025

Unterschrift StudentIn

Unterschrift BetreuerIn

Zusammenfassung

Die Cabibbo-Kobayashi-Maskawa (CKM)-Matrix ist die Hauptquelle der CP-Verletzung im Standardmodell (SM) der Teilchenphysik, die für die Materie-Antimaterie-Asymmetrie notwendig ist. Präzise Messungen des CKM-Matrixelements $|V_{cb}|$ spielen eine entscheidende Rolle bei der Überprüfung des SM und der Bestimmung des CP-Verletzungsparameters. Allerdings deuten Diskrepanzen zwischen der Bestimmung von $|V_{cb}|$ aus exklusiven und inklusiven semileptonischen Zerfällen auf die Existenz unbekannter Effekte hin.

Um diese Diskrepanz weiter zu untersuchen, zielt diese Arbeit darauf ab, $|V_{cb}|$ zu bestimmen, indem kürzlich berechnete theoretische Vorhersagen für q^2-Momente an experimentelle Daten aus inklusiven semileptonischen Zerfällen $B \to X_c l \nu_l$ angepasst werden.

Das theoretische Modell basiert auf der Operator-Product-Expansion (OPE), welche es ermöglicht, das Produkt von Operatoren an verschiedenen Raumzeitpunkten als eine Reihe lokaler Operatoren darzustellen. Durch eine doppelte Entwicklung in der starke Kopplungskonstante α_s und der inversen Bottom-Quark-Masse Λ_{QCD}/m_b hängen die Momente von den störungstheoretischen Koeffizienten und nicht-störungstheoretischen Matrixelementen der lokalen Operatoren ab. Diese Matrixelemente, bekannt als Heavy-Quark-Expansion-(HQE)-Parameter, müssen durch das Fitverfahren extrahiert werden.

Der experimentelle Input besteht aus dem quadrierten Impulsübertrag des Lepton-Neutrino-Paares q^2, der in den Experimenten Belle und Belle II gemessen wurde. Ein wesentlicher Aspekt dieser Arbeit ist das Fit-Verfahren, das theoretische Unsicherheiten der Berechnungen sowie externe Randbedingungen einbezieht, um das Fit-Ergebnis zu stabilisieren. Zur Validierung des Fit-Verfahrens werden Fits an die Leptonenenergie E_l und der Hadronenmassenverteilung m_X^2 durchgeführt sowie ein Fit der zusätzlich q^2-Daten enthält. Diese Ergebnisse werden mit mit publizierten Resultaten verglichen. Die m_X^2 und E_l Momente wurden in den Experimenten BaBar, Belle, CDF, CLEO und DELPHI gemessen.

Die globalen Fits werden mit einem Maximum-Likelihood-Schätzverfahren durchgeführt, das mit dem `Minuit`-Framework implementiert wurde. Die erste Extraktion von $|V_{cb}|$ führte zu großen Unsicherheiten, da die q^2-Momente unempfindlich gegenüber dem HQE-Parameter μ_π^2 sind. Mit zusätzlichen Restriktionen aus anderen Fits konnte der q^2-Fit stabilisiert werden. Die finale Fit mit nur q^2-Momenten ergibt

$$|V_{cb}| = (42,15 \pm 0,54) \times 10^{-3}.$$

Dieses Ergebnis ist konsistent mit vorherigen inklusiven Bestimmungen von $|V_{cb}|$ und zeigt, dass $|V_{cb}|$ zuverlässig mit q^2-Momenten bestimmt werden kann.

Eine Analyse der anderen HQE-Parameter zeigt Diskrepanzen zwischen den Fit-Typen. Während der Fit mit ausschließlich q^2-Momente für die meisten HQE-

Parameter kompatible Werte liefert, gibt es Unterschiede in den Ergebnissen für ρ_D^3. Dies deutet auf mögliche theoretische oder experimentelle Probleme in der Behandlung dieser Momente hin, die weiterer Untersuchungen erfordern.

Abstract

The Cabibbo-Kobayashi-Maskawa (CKM) matrix is the primary source of CP violation in the Standard Model (SM) of particle physics, which is necessary for a matter-antimatter asymmetry. Precise measurements of the CKM matrix element $|V_{cb}|$ play an important role in testing the SM and determining the CP violation parameter. However, discrepancies between the determination of $|V_{cb}|$ from exclusive and inclusive semileptonic decays suggest the existence of unknown effects.

To gain further insight into this discrepancy, this thesis aims to determine $|V_{cb}|$ by fitting recently computed theoretical predictions for q^2 moments to experimental data from inclusive semileptonic decays $B \to X_c l \nu_l$.

The theoretical model is based on the operator product expansion (OPE), which allows for a product of operators at different points in spacetime to be expressed as a series of local operators. By performing a double expansion in the strong coupling constant α_s and the inverse bottom quark mass Λ_{QCD}/m_b, the moments depend on perturbative coefficients and non-perturbative matrix elements of these local operators. These matrix elements, known as the Heavy Quark Expansion (HQE) parameters, must be extracted by the fit.

The experimental input consists of the squared momentum transfer of the lepton-neutrino pair q^2 measured at the Belle and Belle II experiments. A key aspect of this study is the fitting procedure, which includes the theoretical errors of the calculations and external constraints to stabilize the fit. To validate the fitting procedure fits to the lepton energy E_l and the hadron mass distribution m_X^2 as well as a fit including q^2 data are performed and compared with published results. The m_X^2 and E_l moments have been measured at the BaBar, Belle, CDF, CLEO, and DELPHI experiments.

The global fits are performed using a maximum likelihood estimation technique implemented with the `Minuit` framework. The first extraction of $|V_{cb}|$ led to large uncertainties since the q^2 moments are insensitive to the HQE parameter μ_π^2. With additional constraints obtained from other fits, the q^2 fit could be stabilized. The final fit using only q^2 moments results in

$$|V_{cb}| = (42.15 \pm 0.54) \times 10^{-3}.$$

This result is consistent with previous inclusive determinations of $|V_{cb}|$ and demonstrates that $|V_{cb}|$ can be reliably determined using q^2 moments.

An analysis of the other HQE parameters reveals discrepancies between fit types. While the fit using only q^2 moments yields compatible values for most of the HQE parameters, there are differences in the results for ρ_D^3. This suggests potential theoretical or experimental problems in the treatment of these moments that require further investigation.

Contents

Chapter 1

Introduction

One of the thoroughly tested theories in modern physics is the Standard Model (SM) of particle physics. It describes the fundamental particles and their interactions, which govern the behavior of matter in the universe. The SM describes three forces — electromagnetic, weak, and strong force — as quantum field theories (QFT), but does not include gravity. Not only is the theory behind the SM impressive, but it can compete with today's most precise high-energy experiments. One of the latest milestones in high-energy physics was the discovery of the Higgs particle, proposed by P. Higgs in 1964 [1]. However, at that time, the experiments were not yet able to prove the existence of this new particle. It took almost 60 years for experimental physics to catch up with theoretical physics. In 2012, scientists at CERN successfully demonstrated the existence of the Higgs particle [2]. Scientists continue to attempt to disprove the predictions of the SM and develop new theories to advance our understanding of the universe and its smallest components. Theories proposed to explain unsolved problems, such as the matter-antimatter asymmetry in the universe, include new particles and processes that would lead to deviations from the SM. To explain the observed matter-antimatter asymmetry, A.D. Sakharov formulated three conditions: (i) violation of the baryon number: (ii) C and CP violation; and (iii) departure from the thermal equilibrium [3]. CP symmetry states that the combination of charge conjugation (C), which interchanges a particle with its antiparticle, and parity (P), which inverts the spatial coordinates of the particles, leaves the laws of physics unchanged. Without CP symmetry violation, every process that generates more matter than antimatter would have a conjugate process producing the opposite effect, preventing the necessary asymmetry from arising. Therefore, CP violation is a fundamental requirement in any theory describing the forces that govern our Universe.

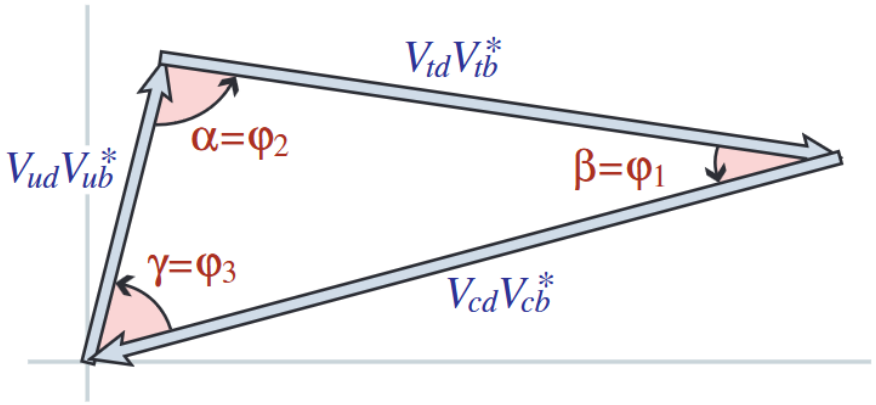

Figure 1.1: Graphical representation of the unitarity constraint $V_{ud}V_{ub}^* = V_{cd}V_{cb}^* + V_{td}V_{tb}^* = 0$. Image taken from reference [5].

CP Violation in the SM

In the SM, the Cabibbo-Kobayashi-Maskawa (CKM) matrix, which describes quark mixing, is the source of CP violation [4]. The elusiveness of the neutrinos makes them difficult to detect, so high-energy physics experiments focus more on the CKM matrix. The unitary 3×3 CKM matrix relates the weak eigenstates to the mass eigenstates of the down-type d, s and b quarks. CP violating effects enter the CKM matrix through a complex phase. However, measurements of these effects show that they are not sufficient to explain the matter-antimatter asymmetry and that additional sources of CP violation are required [5]. In New Physics (NP) scenarios additional heavy particles could introduce further CP violating effects. If these new particles couple to quarks, the SM predictions might differ from measurements of the CKM parameters that constrain the unitary condition of the CKM, illustrated in Figure 1.1. For this, a precise determination of the CKM parameters, like V_{cb} is required.

The magnitude of V_{cb} can be measured through semileptonic decays $b \to cl\overline{\nu}_l$, as they provide a clean and precise way for extraction. The leptonic part of the decay is well understood theoretically and the charged lepton in the final state can be directly measured in experiments. In pure hadronic decays, the effects of the strong interaction significantly complicate the analysis. The total decay at tree-level is proportional to $|V_{cb}|^2$ and offers an experimental accessible and theoretically predictable way to measure the CKM parameter.

Semileptonic Decays

Semileptonic B decays of the form of $B \to Xl\overline{\nu}_l$ can be categorized into two groups: exclusive decays, where the final state hadron X is a specified meson ($X = D, D^*, \pi$,...); or inclusive decays, where all possible hadronic states X are summed over. The theoretical predictions for exclusive decays rely on non-perturbative calculations of form factors that compute the low-energy dynamics of the strong force. The non-perturbative nature of Quantum Chromodynamics (QCD) at low energies complicates this approach immensely. On the other hand, inclusive decays use the Heavy Quark Expansion (HQE) to express the total decay rate as an expansion in Λ_{QCD}/m_b, the inverse mass of bottom quark m_b and the energy scale of QCD Λ_{QCD}. At each order of Λ_{QCD}/m_b, the expansion depends on Wilson coefficients, which are perturbatively calculated, and non-perturbative matrix elements. The theoretical model of the matrix elements is based on the Operator Product Expansion (OPE). In addition to the total decay rate, various observables can also be expanded with the same set of non-perturbative parameters. These matrix elements are determined by fitting theoretical predictions to experimental data

Determination of V_{cb}

References [6, 7] use the experimentally measured distribution of the lepton energy distribution E_l and hadronic invariant mass spectrum m_X^2 to determine the HQE parameters with a fit. The total semileptonic width is used for the extraction of $|V_{cb}|$. Perturbative corrections to the Wilson coefficients are calculated up to orders of $\mathcal{O}(1/m_b^3)$, $\mathcal{O}(\alpha_s/m_b^2)$, $\mathcal{O}(\alpha_s^2)$ (for the moments) and $\mathcal{O}(\alpha_s^3)$ (for the total semileptonic width). The specific references for the corrections are provided in [6, 7].

The proliferation of the non-perturbative matrix elements at higher order makes their extraction challenging, so an alternative method based on Reparametrization Invariance (RPI) was proposed in reference [8]. This reduces the number of independent operators at $\mathcal{O}(1/m_b^4)$ from thirteen to eight, but holds valid only for the leptonic invariant mass spectrum q^2. The value of $|V_{cb}|$ extracted from a fit based on RPI and only q^2 moments agrees with other inclusive fits, but the change in the basis for the HQE parameters makes it difficult to compare them to other fits [9]. The inclusion of the recently computed q^2 moments, without RPI, in reference [10] to the fits on E_l & m_X^2 moments allows for a cross-check, to see whether the q^2 moments are compatible with other determination.

The most precise determinations of $|V_{cb}|$ from both the exclusive and inclusive methods are shown in Figure 1.2. The values reported by the Particle Data Group (PDG) for the inclusive and exclusive determinations differ by three standard deviations, a discrepancy known as the V_{cb} puzzle [15]. Recent exclusive determination of $|V_{cb}|$ from the decay $B \to D^* l\bar{\nu}_l$ are in better agreement with the inclusive value, but a tension still persists.

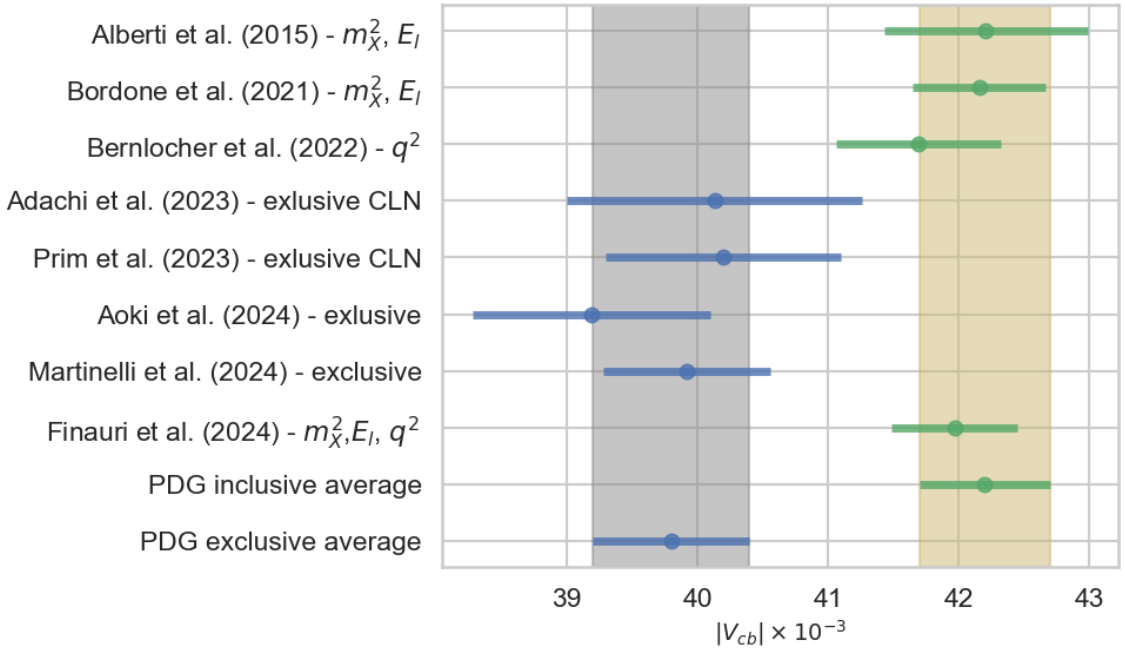

Figure 1.2: Recent values of $|V_{cb}|$ determined with exclusive (blue) and inclusive (green) methods. The shaded areas are exclusive (gray) and inclusive (beige) averages from the Particle Data Group (PDG) [5]. For the exclusive values from Adachi et al. [11] and Prim et al. [12] only the value for Caprini-Lellouch-Neubert (CLN) parametrization is taken. The exclusive $|V_{cb}|$ values from Aoki et al. [13] and Martinelli et al. [14] were measured with $B \to D^* l \nu_l$ decays. The inclusive determination of Alberti et al. [6] and Bordone et al. [7] use m_X^2 and E_l moments for their fits. Finauri et al. [10] uses the q^2 moments, in addition to m_X^2 and E_l moments. The fit of Bernlocher et al. [9] uses methods based on the RPI and only q^2 moments.

Thesis Objectives and Structure

As of the writing of this thesis, no results have been published for a fit based solely on q^2 moments, using the same methods as those applied to the E_l and m_X^2 moments. Investigating a fit based exclusively on q^2 moments could provide further insight into resolving the V_{cb} puzzle.

The aim of this thesis is to perform a fit based on only q^2 moments, with the theoretical q^2 computations from reference [10]. The results will be compared to previous findings from inclusive semileptonic decays to check for compatibility. Fits on E_l, m_X^2 and q^2 moments will also be performed to verify whether the methods used in this thesis align with those in references [7, 10].

This thesis is structured as follows: Chapter 2 gives an overview of the SM and introduces the theoretical description of the OPE, HQE and semileptonic B decays. The particle accelerators and detectors, where the data used in this thesis was measured, are described in Chapter 3, with a special focus on the Belle II detector, as the q^2 data employed in this thesis were measured at Belle and Belle II. In Chapter 4 the basics for reconstructing $B \to X_c l \nu_l$ decays are explained, and the moments used for fits in this thesis are defined. Chapter 5 explains the fit procedure of this thesis in detail, as well as the computation of the theoretical covariant matrix and the individual corrections to the computations and measurements. The fits on $E_l \& m_X^2$ and $E_l, m_X^2 \& q^2$ moments are used to validate the fit procedure and are presented in Chapter 6. The results from the fit on only q^2 moments are presented in Chapter 7. A summary of the results and a conclusion are provided in Chapter 8. Additionally, an outlook and suggestions for future experiments and analyses are offered.

Chapter 2

Theory

This chapter introduces the theoretical concepts for determining $|V_{cb}|$ from inclusive $B \to X_c l\nu$. Sections 2.1 and 2.2 define natural units as a measurement system and provide a brief overview of the Standard Model of particle physics (SM), following the descriptions in references [16, 17]. Sections 2.3 and 2.6 cover the particle of interest, the B meson, and its inclusive semileptonic decay. The derivation of the total decay rate is based on the discussions presented in references [18, 19].

The theoretical concepts and mathematical formulations that enable the calculation of the different moments E_l, m_X and q^2 are presented in Sections 2.4 and 2.5. Finally, Section 2.7 introduces the individual scales at which the parameters are evaluated in the fits.

2.1 Natural Units

When dealing with physics at the scale of subatomic particles, one often encounters the challenge of handling quantities with very large or very small exponents. For example, the mass of a single proton is 1.67×10^{-27} kg when expressed in S.I. units. To better reflect the natural scales of particle physics and simplify algebraic expressions, physicists use natural units. This system of units is based on the convention of setting:

$$\hbar = c = 1, \tag{2.1}$$

where $\hbar = 1.055 \times 10^{-34}$ J s is the reduced Planck constant, and $c = 2.998 \times 10^{8}$ m s^{-1} is the speed of light in vacuum [16]. In natural units, the conventional SI base units [kg,m,s] are replaced by [$\hbar$, c, GeV]. Consequently, all physical quantities are expressed as powers of GeV with 1 GeV $= 1.602 \times 10^{-10}$ J. Table 2.1 illustrates two of the most common quantities used in this thesis, energy and mass, and their respective representations in SI and natural units. In natural units, energy and mass share the same unit, simplifying many calculations in particle physics.

Quantity	S.I.	Natural Unit
Energy	$\mathrm{kg\,m^2\,s^{-2}}$	GeV
Mass	kg	GeV

Table 2.1: The two most common quantities of this thesis in S.I. and natural units.

For the remainder of this work, all values will be expressed using natural units unless specified otherwise.

2.2 Standard Model of Particle Physics

The SM is a quantum field theory with an invariance under local transformations defined by the $SU(3)\times SU(2)\times U(1)$ gauge group. $SU(n)$ refers to the special unitary group, consisting of $n\times n$ unitary matrices with a determinant of 1. A gauge group is a mathematical description of the theory's symmetries, which governs the behavior of elementary particles and their interactions.

Each invariance describes an interaction between the fundamental particles and can be formulated as an individual theory. The $SU(3)$ invariance governs the strong interaction of particles with a color charge, described by Quantum Chromodynamics (QCD). It explains the formation of hadrons, such as protons and neutrons and how these particles combine to form atomic nuclei. Phenomena like the β-decay and electromagnetism require the introduction of the weak interaction and Quantum Electrodynamics (QED). These two interactions are unified under the $SU(2)\times U(1)$ gauge group, which manifests itself as the electroweak interaction [20, 21, 22].

Elementary particles that constitute matter are classified into two categories: half-integer spin particles called fermions and integer spin particles called bosons. The latter transmits the strong, weak and electromagnetic interaction between fermions. There are a total of 13 bosons: 8 gluons g that mediate the strong force, $W^{\pm}$ and Z that mediate the weak force, the photon γ that mediates the electromagnetic force and the Higgs boson H. While photons and gluons are massless particles, the $W^{\pm}$ and Z bosons have masses of $m_W = (80.3692 \pm 0.0133)$ GeV and $m_Z = (91.188 \pm 0.002)$ GeV [5].

Fermions are further subdivided into quarks and leptons, each appearing in three generations. The first generation of quarks are up u and down d quarks with a charge of $2/3$ and $-1/3$ of the elementary charge e. For leptons electrons e^- and electron-neutrinos ν_e count to the first generation. The second and third generation of particles have the same properties as the first generation except for their heavier mass. The properties of the individual fermions are determined by their type, which is also referred to as flavor. Quarks and leptons also have corresponding antiparticles, which have the same mass as their counterparts but opposite electric charge and

magnetic moment. Antiparticles are often denoted with a bar, e.g., anti-$u \rightarrow \overline{u}$.

To complete the SM, an additional mechanism is required for it to be consistent: the Higgs mechanism [1]. Through interactions with the Higgs field, particles acquire their masses. This explains why the $W^{\pm}$ and Z bosons have a mass while the photon γ and gluons g remain massless, as they couple to the Higgs field. The excitation of the Higgs field corresponds to a spin-0 particle, the Higgs boson H. Figure 2.1 summarizes all particles in the SM, showing their masses, electric charges, and spins.

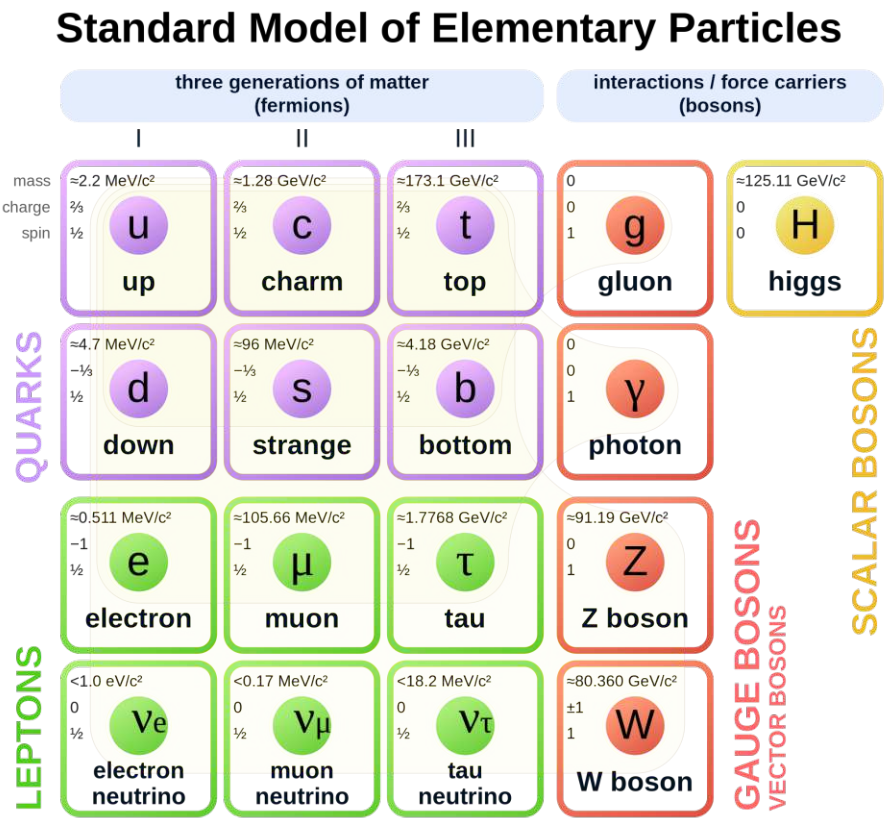

Figure 2.1: Illustration of the SM's individual particles with their masses, electric charge and spin shown. [23]

The properties of the interactions are different from each other at low enough energies. The gauge bosons of the strong and electromagnetic interaction are massless, but the potential of the photon described by QED is $V_{QED} \propto 1/r$, whereas the QCD potential for the gluons is $V_{QCD} \propto r$. This implies that a separation of two quarks would require an infinite amount of energy, a phenomenon known as confinement. Consequently, quarks are only observed as part of bound, color-neutral hadronic states, such as protons and neutrons. Interactions can also be categorized

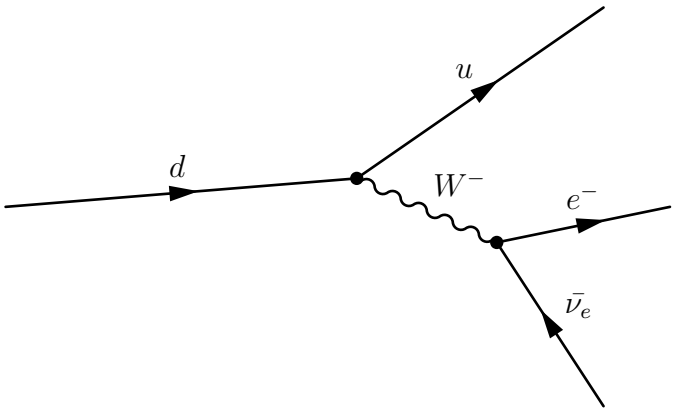

Figure 2.2: Lowest order Feynman diagram of the β^- decay.

by dimensionless coupling constants. In the case of QED, the fine-structure constant $\alpha \approx 1/137$ describes the electromagnetic coupling strength. For the strong interaction, only quarks couple to the gluons with a coupling constant of α_S, as they are the only fermions to carry the color charge of QCD.

Flavor changes in quarks occur through weak decays, mediated by the W boson. For instance, in β decays $d \to u + e^- + \overline{\nu}_e$, a d quark transforms into a u quark by emitting a virtual W^- boson, shown in Figure 2.2. The transition amplitude for such decays includes terms proportional to m_W which suppresses weak decays at lower energies. However, at higher energies, the weak force dominates over the electromagnetic interaction due to its coupling constant α_W, being approximately 1/30. Transitions can not only occur within one generation, but also between generations. The strength of the transitions is defined by the unitary Cabibbo-Kobayashi-Maskawa (CKM) matrix, which connects the weak eigenstates to the mass eigenstates of the quarks:

$$\begin{pmatrix} d' \\ s' \\ b' \end{pmatrix} = \begin{pmatrix} V_{ud} & V_{us} & V_{ub} \\ V_{cd} & V_{cs} & V_{cb} \\ V_{td} & V_{ts} & V_{tb} \end{pmatrix} \begin{pmatrix} d \\ s \\ b \end{pmatrix}, \tag{2.2}$$

with $'$ denoting the weak eigenstates.

Using the freedom of phase redefinitions for the quark fields, the CKM matrix has three rotation angles and one CP violation-inducing phase [24]. The CKM matrix element $|V_{cb}|$ in equation 2.2 plays a critical role in semileptonic decays. It gives the relative probability that a b quark decays into a c quark.

The unitary condition for the CKM matrix $\mathbb{I} = V_{CKM}^{\dagger} V_{CKM}$ leads to relations like:

$$V_{ub}V_{ub}^* + V_{cb}V_{cb}^* + V_{tb}V_{tb}^* = 0. \tag{2.3}$$

Dividing equation 2.3 by $V_{cb}V_{cb}^*$ and defining new parameters $\overline{\rho}$ and $\overline{\eta}$ as

$$\overline{\rho} + i\overline{\eta} = -\frac{V_{ub}V_{ub}^*}{V_{cb}V_{cb}^*}, \tag{2.4}$$

this connection can be illustrated as a triangle within the complex plane as is shown in Figure 2.3 [25, 24]. The exact value of the CKM parameter $|V_{cb}|$ is crucial as it normalizes this unitary triangle.

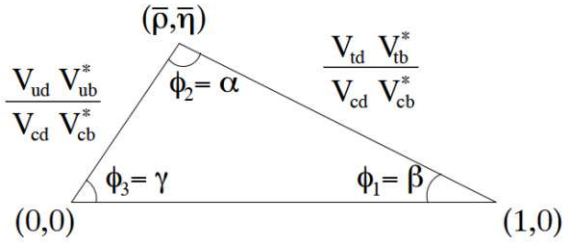

Figure 2.3: Illustration of the unitary triangle [24].

2.3 B Mesons

Quarks are always bound together due to the phenomenon of confinement, which prevents them from existing as free particles in normal conditions. These bound states of two or more quarks are collectively called hadrons. A specific subclass of hadrons is the mesons, which are composite particles made up of exactly two quarks: a quark and an antiquark. Mesons are typically identified by their heavier quark. For example, the B meson contains a bottom quark b paired with a quark of lower mass. Table 2.2 summarizes the ground state B mesons, their corresponding antiparticles, quark compositions and masses.

B Meson	**Antiparticle**	**Quarks**	**Mass** GeV
B^+	B^-	$u\bar{b}$	5.279
B^0	$\overline{B}^0$	$d\bar{b}$	5.280
B_s^0	$\overline{B}_s^0$	$s\bar{b}$	5.367
B_c^+	B_c^-	$c\bar{b}$	6.275

Table 2.2: Summary of the ground state B mesons, their antiparticles, quark compositions, and masses [5].

Due to their wide range of decay channels, B mesons serve as ideal candidates for studying rare decays and testing the limits of the Standard Model. These rare

decays can be influenced by virtual particles or interactions that lie outside the predictions of the SM, providing a window into potential New Physics (NP).

Hadrons with a b and $\bar{b}$ quarks are called bottomonium. An overview of the bottomonium spectrum is shown in Figure 2.4, with the threshold energy for $B\overline{B}$ pair marked. The most effective way to create B mesons is the $\Upsilon(4S)$ resonance, which corresponds to an energy of 10.58 GeV, as it decays almost exclusively into charged or neutral B meson pairs [24].

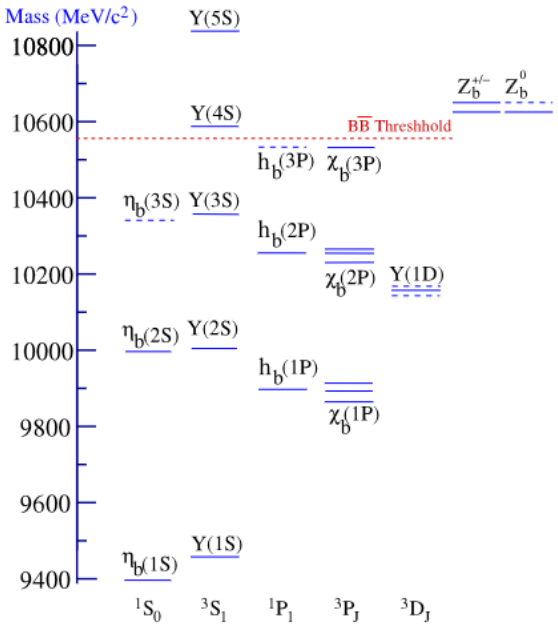

Figure 2.4: Spectrum of bottomonium, with the $B\overline{B}$ pair threshold marked. [24]

Additionally, the decay properties of B mesons are instrumental in determining fundamental parameters of the SM, such as the elements of the CKM matrix, which describe the mixing and transitions between quark flavors.

2.4 Operator Product Expansion (OPE)

The operator product expansion (OPE), developed by K. Wilson, provides a method to represent a product of two operators at different spacetime as a series of simpler operators at a single spacetime [26]. When considering the time-ordered product $TA(x)B(0)$, ultra-violet divergences emerge in the limit of $x^\mu \to 0$, where the space-time separation between the operators vanishes. To address these divergences for small x, the product can be expanded as a series of local operators:

$$TA(x)B(0) = \sum_k C_k(x,\mu)O_k(0) \tag{2.5}$$

where μ is the renormalization scale at which the theory is valid, O_k are local operators and C_k are the Wilson coefficients [19, 27, 26]. The two key components of this expansion, the Wilson coefficients, and the local operators encapsulate distinct physical information:

1. **Wilson coefficients** encode the effects of the interactions at short-distances, which are equal to high energy. These coefficients depend on μ and are calculated perturbatively in most cases.

2. **Local operators** contain the long-distance effects, which are equal to low-energy. They are reconstructed from the fields and derivatives that are present in the theory of interest. They are sensitive to the large-scale structure of the system and are non-perturbative by nature.

2.5 Heavy Quark Physics

All flavor-changing processes involve the weak interaction mediated by the massive W boson. Additionally, the B mesons contain a heavy b quark and a much lighter quark q. This provides an opportunity to examine an effective theory by integrating out the W boson and expanding in powers of $1/m_b$, where m_b is the mass of the bottom quark. The following sections describe the steps for developing the Heavy Quark Effective Theory (HQET).

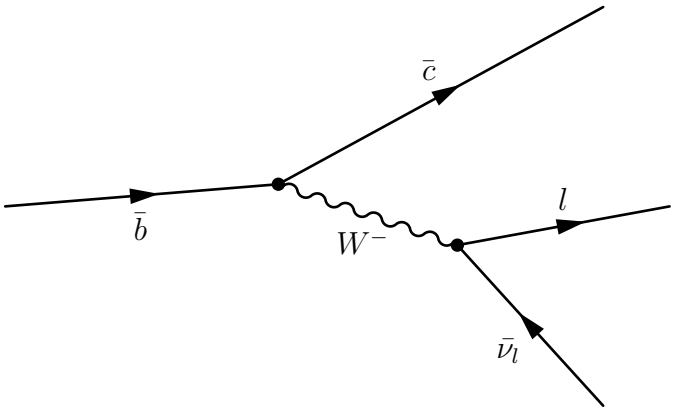

Figure 2.5: Lowest order Feynman diagram of the semileptonic weak decay $\bar{b} \to \bar{c} + l + \bar{\nu}_l$.

2.5.1 Effective Hamiltonian for weak decays

Weak decays mediated by the W boson, as shown in the Feynman diagram in Figure 2.5, involve a propagator of the form:

$$\frac{1}{q^2 - m_W^2}\left(g_{\mu\nu} - \frac{q_\mu q_\nu}{m_W^2}\right), \tag{2.6}$$

where $q = (p_b - p_c)$ is the four-momentum of the virtual W boson, and p_b and p_c represent the four-momenta of the bottom and charm quarks, respectively. At energy scales much below m_W the momenta p of the quarks is much smaller than m_W. Therefore, the denominator $(q^2 - m_W^2)$ can be approximated by $-m_W^2$. Neglecting the factor of $q_\mu q_\nu / m_W^2$ in the nominator simplifies the propagator to:

$$-\frac{g_{\mu\nu}}{m_W^2} \tag{2.7}$$

This approximation removes any dependence on q, and the tree-level amplitude for the decay $\overline{b} \to \overline{c} + l + \overline{\nu_l}$ can now be described by the following local effective Hamiltonian:

$$H_W = \frac{4G_F}{\sqrt{2}} V_{cb} (\bar{c}\gamma^\mu P_L b)(\bar{l}\gamma_\mu P_L \nu_l), \tag{2.8}$$

where $G_F/\sqrt{2} = g_W^2/8m_W^2$ defines the Fermi constant G_F and g_W is the coupling strength of the weak interaction.

2.5.2 Heavy Quark Effective Theory (HQET)

The mass of the bottom quark m_b is larger than other parameters, like the transfer momentum q and the light quark masses m_q, appearing in a semileptonic decay. Therefore, it is convenient to expand the theory in $1/m_b$. This would lead to a Lagrangian like:

$$\mathcal{L} = \mathcal{L}_0 + \frac{1}{m_b}\mathcal{L}_1 + \frac{1}{m_b^2}\mathcal{L}_2 + ..., \tag{2.9}$$

with $\mathcal{L}_0$ being the leading contribution and all other contributions $\mathcal{L}_i$ being suppressed by power of $1/m_b^i$. The steps to get this kind of expansion are laid out in this section and follow the instructions in [28, 19].

The first step is to examine the size of the interactions that a b quark experiences. For a heavy quark in a meson, its interactions with a light quark are of the order $\mathcal{O}(\Lambda_{QCD})$, where Λ_{QCD} represents the energy scale at which QCD becomes strongly coupled. Because $\Lambda_{QCD} \ll m_b$, the bottom quark in a meson carries most of the

momentum and can be expressed as $p^\mu = m_b v^\mu$, where v represents the velocity of the quark.

To obtain the effective Lagrangian, the starting point is to write any heavy quark field Q in terms of velocity-dependent fields as:

$$Q(x) = e^{-im_Q v\cdot x}(Q_v(x) + \mathcal{Q}_v(x)), \tag{2.10}$$

with

$$Q_v(x) = e^{im_Q v\cdot x}\frac{1+\not{v}}{2}Q(x), \qquad \mathcal{Q}_v(x) = e^{im_Q v\cdot x}\frac{1-\not{v}}{2}Q(x) \tag{2.11}$$

Here, the factor $(1+\not{v})/2$ is a velocity-dependent projector that isolates the component of the field $Q(x)$ corresponding to the heavy quark's velocity, while the factor $(1-\not{v})/2$ isolates the component from the interactions. This projector becomes $(1\pm\gamma^0)$, in a frame where the heavy quark is at rest.

Inserting these terms in the QCD Lagrangian results in:

$$\mathcal{L} = \overline{Q}(i\not{D} - m_Q)Q = \overline{Q}_v(i\not{D})Q_v - \overline{\mathcal{Q}}_v(-i\not{D} + 2m_Q)\mathcal{Q}_v + \overline{Q}_v i\not{D}\mathcal{Q}_v + \overline{\mathcal{Q}}_v i\not{D}Q_v, \tag{2.12}$$

using $\not{v}Q_v = Q_v$ and $\not{v}\mathcal{Q}_v = -\mathcal{Q}_v$. Furthermore, the γ^μ in the first two terms can be replaced by $\pm v^\mu$. This can be shown by inserting $(1\pm\not{v})/2$ before and after the γ^μ:

$$\frac{1\pm\not{v}}{2}\gamma^\mu\frac{1\pm\not{v}}{2} = \pm v^\mu\frac{1\pm\not{v}}{2} \tag{2.13}$$

Since the projectors $(1\pm\not{v})/2$ are identity projectors of the fields Q_v and $\mathcal{Q}_v$, they leave the fields unchanged. Therefore, γ^μ can be replaced by v^μ in the first term and $-v^\mu$ in the second term.

For convenience, four-vectors can be split into components parallel and perpendicular to the velocity v:

$$X^\mu = X^\mu_\perp + X\cdot v v^\mu \tag{2.14}$$

This simplifies the Lagrangian to:

$$\mathcal{L} = \overline{Q}(iv\cdot D - m_Q)Q = \overline{Q}_v(i\not{D})Q_v - \overline{\mathcal{Q}}_v(iv\cdot D + 2m_Q)\mathcal{Q}_v + \overline{Q}_v i\not{D}_\perp\mathcal{Q}_v + \overline{\mathcal{Q}}_v i\not{D}_\perp Q_v \tag{2.15}$$

This form of the Lagrangian shows that the $\mathcal{Q}_v$ fields correspond to an excitation with mass $2m_Q$, which is the minimum energy that is required for a heavy quark-antiquark pair. Since the HQET is only valid at energy scales lower than this threshold, the field $\mathcal{Q}_v$ can be integrated out. At tree-level, the equation of motions for $\mathcal{Q}_v$ can be solved to express it in terms of Q_v:

$$(iv \cdot D + 2m_Q)\mathcal{Q}_v = i\not{D}_\perp Q_v \tag{2.16}$$

Substituting the expression for $\mathcal{Q}_v$ into the Lagrangian 2.15 and expanding in $1/m_Q$ results in:

$$\begin{aligned}\mathcal{L} &= \overline{Q}_v(i\not{D} + i\not{D}_\perp \frac{1}{2m_Q + iv \cdot D} i\not{D}_\perp)Q_v \\ &= \overline{Q}_v(i\not{D} - \frac{1}{2m_Q}\not{D}_\perp \not{D}_\perp)Q_v + \mathcal{O}\left(\frac{1}{m_Q^2}\right)\end{aligned} \tag{2.17}$$

Thus, the Lagrangian is expanded in the order of $1/m_Q$ and is also only dependent on the heavy quark field Q_v. It is important to note that here only tree-level calculations were used and that loop corrections introduce a dependency on the energy scale μ.

2.6 Inclusive Semileptonic Decays

Inclusive semileptonic decays with B mesons take the form of $B \to X_c l \overline{\nu_l}$, where X_c represents a hadron containing a charm quark c. Inclusive decays refer to processes where no specific final state X_c or $l\overline{\nu_l}$ is identified; instead, all possible final states are summed up. Semileptonic decays are characterized by the presence of a lepton pair $l + \overline{\nu}_l$ in the final state. These flavor-changing interactions are governed by the weak interaction, with the effective Hamiltonian already derived in equation 2.8.

The differential decay rate for these processes in the B meson rest frame is given by:

$$\frac{d\Gamma}{dq^2 dE_l dE_{\nu_l}} = \frac{1}{4}\sum_{X_c}\sum_{\text{lepton spins}} \frac{|\langle X l\overline{\nu}_l| H_W |\overline{B}\rangle|^2}{2m_B}(2\pi)^3\delta^4(p_B - (p_l + p_{\nu_l}) - p_{X_c}), \tag{2.18}$$

where H_W is the effective weak Hamiltonian, and δ^4 ensures the conservation of four-momentum. All possible hadronic states and lepton spins are added up.

In the first approximation, the matrix element in equation 2.18 can be factorized into a leptonic and a hadronic matrix element. This factorization is justified by the observation that the leptons and hadrons interact only via the electroweak force, with no direct interaction through the strong force. Consequently, corrections arising from their interactions are suppressed by the powers of the Fermi constant G_F or the fine-structure constant α. The factorized differential decay rate can thus be written as:

$$\frac{d\Gamma}{dq^2 dE_l dE_{\nu_l}} = 2G_F^2 |V_{cb}|^2 W_{\alpha\beta} L^{\alpha\beta} \tag{2.19}$$

with the general leptonic tensors, encapsulating the properties of the lepton pair, being:

$$L^{\alpha\beta} = 2(p_l^\alpha p_{\nu_l}^\beta + p_l^\beta p_{\nu_l}^\alpha - g^{\alpha\beta} p_l \cdot p_{\nu_l} - i\epsilon^{\eta\beta\lambda\alpha} p_{l\eta} p_{\nu_l \lambda}), \tag{2.20}$$

and the hadronic tensor, describing the contributions from the B meson and hadronic final state, being:

$$W^{\alpha\beta} = \sum_{X_c} (2\pi)^3 \delta^4(p_B - (p_l + p_{\nu_l}) - p_{X_c}) \frac{\langle \overline{B}(p_B)| J^{\dagger\alpha} |X_c(p_{X_c})\rangle \langle X_c(p_{X_c})| J_L^\beta |\overline{B}(p_B)\rangle}{2m_B}. \tag{2.21}$$

Here, $J_L^\alpha = \bar{c}\gamma^\alpha P_L b$, represents the left-handed current. The dependencies on p_B and p_{X_c} are explicitly shown, with the δ function enforcing momentum conservation.

The hadronic tensor $W^{\mu\nu}$ can be written in terms of the imaginary part of the forward scattering amplitude $T^{\mu\nu}$ using the optical theorem:

$$W^{\mu\nu} = -\frac{1}{\pi} \mathrm{Im} T^{\mu\nu} = \frac{1}{\pi} \mathrm{Im} \left(i \int d^4x e^{-iq\cdot x} \frac{\langle \overline{B}| T[J_L^{\dagger\alpha}(x) J_L^\beta(0)] |\overline{B}\rangle}{2m_B} \right) \tag{2.22}$$

The optical theorem relates the total decay rate to the forward scattering amplitude and applies only to inclusive decays, where all final states are summed up [29].

The time-ordered product of operators in equation 2.22 forms the basis of an OPE. By using the heavy quark field defined in equation 2.11, the OPE allows the decay rate to be expanded in powers of $1/m_b$, the inverse of the b quark mass. After performing the expansion and integrating over all free parameters, the total decay rate takes the form of:

$$\Gamma = \Gamma_0 + \frac{1}{m_b}\Gamma_1 + \frac{1}{m_b^2}\Gamma_2 + ... \tag{2.23}$$

At each order of $1/m_b$ the Γ_i are related to matrix elements of local operators:

$$\Gamma_i = \sum_n C_i^{(n)} \langle \overline{B}| \mathcal{O}_i^n |\langle B|\rangle . \tag{2.24}$$

Here, the $\mathcal{O}_i^n$ are operators with mass dimension $i+3$ and $C_i^{(n)}$ are Wilson coefficients, encapsulating short-distance effects. The sum goes over all operators at a given order.

The matrix elements can be determined by dimensional analysis using all available operators of the underlying theory. These parameters are also called HQE parameters. The $i = 0$ contribution to width in equation 2.23 corresponds to the parton model, where the b quark is treated as a free particle. For $i = 1$, dimension-four operators could contribute, but in this theory, there are no such operators. Therefore, the $i = 1$ contribution to the expansion vanishes and there are no $1/m_b$ terms. The first non-trivial contributions arise at $i = 2$, with dimension-five operators. There are two contributions available:

$$\mu_\pi^2 = \frac{\langle \overline{B}(v)| \, \bar{b}_v (iD)^2 b_v \, |\overline{B}(v)\rangle}{2m_b}, \tag{2.25}$$

and

$$\mu_G^2 = -\frac{\langle \overline{B}(v)| \, \bar{b}_v \vec{\sigma} \vec{B} b_v \, |\overline{B}(v)\rangle}{2m_b} + \mathcal{O}(\frac{1}{m_b}). \tag{2.26}$$

Here, the fields b_v are the heavy quark fields defined in equation 2.11, σ are the Pauli matrices and B denotes the background chromoelectric and chromomagnetic fields. The matrix elements for $1/m_b^3$ are defined in [30]. They are the Darwin ρ_D^3 and spin-orbital ρ_{LS}^3 terms. Higher-order contributions ($1/m_b^4$ and beyond) are generally neglected due to the proliferation of non-perturbative matrix elements, which complicates the analysis significantly [31].

Not only can the total decay rate Γ be expanded using HQE, but also various observables M_i, can be expressed in a similar form. The expectation values of these observables is defined as:

$$\langle M_i \rangle = \frac{\int dM_i M_i \frac{d\Gamma}{dM_i}}{\int dM_i \frac{d\Gamma}{dM_i}}, \tag{2.27}$$

and can be expanded as:

$$\langle M_i \rangle = \langle M_i^0 \rangle + \frac{1}{m_b} \langle M_i^1 \rangle + \frac{1}{m_b^2} \langle M_i^2 \rangle + \frac{1}{m_b^3} \langle M_i^3 \rangle + ... \tag{2.28}$$

The same set of HQE parameters that describes the total decay Γ also determines the expansion of $\langle M_i \rangle$.

2.7 Kinetic Scheme and Scales of Parameters

The theories in the previous sections are effective descriptions, meaning they are only valid under specific conditions and energy scales. The OPE, for instance, separates low-energy from high-energy physics, with the Wilson cutoff μ acting as

the energy scale at which this separation occurs. Consequently, all HQE parameters are dependent on the exact value of μ.

This scale dependence is not unique to the HQE parameters. Other physical quantities, such as the observed masses of quarks m_q, are also energy-dependent. This energy dependence arises from renormalization, a process that systematically redefines physical quantities to remove divergences in the theory and make predictions finite. Renormalization introduces a scale μ, which affects how parameters like masses and coupling constants are defined and evaluated [29, 17].

In this thesis, calculations combine two renormalization schemes: the kinetic scheme and $\overline{MS}$ (modified minimal-subtraction) scheme [32, 33]. The HQE parameters μ_π^2, μ_G^2, ρ_D^3 and ρ_{LS}^3, as well as the bottom charm mass m_b, are evaluated in the kinetic scheme. This scheme provides a low-scale mass definition that minimizes uncertainties related to infrared (IR) renormalons, making it particularly suitable for describing heavy quark systems. The charm quark mass m_c, on the other hand, is determined using the $\overline{MS}$ scheme, which is widely used due to its simplicity and consistency in higher-order perturbative calculations.

Another critical scale-dependent parameter is the coupling constant of the strong interaction, α_s. The value of α_s evolves with the energy scale, a phenomenon known as the running of the coupling constant. At higher energies, α_s decreases, reflecting the property of asymptotic freedom in QCD, where quarks interact weakly at short distances. This scale dependence sets the stage for an expansion of the Wilson coefficients in powers of α_s, enabling the perturbative treatment of high-energy contributions in the HQE framework.

To manage the various energy scales involved, distinct subscripts are assigned to the different scales used in the evaluation:

- μ_{kin}, for the scale of the kinetic scheme
- $\mu_{\overline{MS}}$, for the scale of the $\overline{MS}$ scheme
- μ_{α_s}, for the scale of the coupling constant of the strong interaction, α_s

Chapter 3

Experiments

In this thesis, data collected from six experiments—BaBar, Belle, Belle II, CDF, CLEO, and DELPHI—are used to determine $|V_{cb}|$ and the HQE parameters. This chapter provides a concise overview of the fundamentals of high-energy physics experiments.

Section 3.1 introduces key concepts and parameters of particle accelerators and detectors, based on the explanations in references [34, 16, 35]. Sections 3.2 and 3.3 then focus on the individual components of the Belle II detector and its associated accelerator, as Belle II is the only experiment among the six that is still ongoing. Section 3.4 offers a brief overview of the other experiments. Section 3.5 describes the process of combining measurements from individual detector components to identify particles. The role of Monte Carlo (MC) simulations in data analysis and the specific simulation modules used in Belle II are introduced in Section 3.6.

3.1 Basics of Particle Accelerator and Detectors

Particle accelerators have two fundamental components: the particle source and the main accelerator. Particle sources vary depending on the type of particles needed. Ion or proton beams, for instance, are created using a glow discharge that ionizes a gas. For electrons, the most common source is a heated cathode coated with specific materials that reduce the energy required to emit electrons. The creation of antiparticles, such as positrons or antiprotons, is more complex. It involves directing a high-energy electron or proton beam at a heavy metal target. Through interactions with the material and pair production, antiparticles are generated along with other particles.

In the main accelerator, particles must be organized into a specific time structure for effective acceleration. This is achieved by mechanically blocking the beam with a chopper or by deflecting particles using magnetic and alternating electric fields,

forming distinct particle bunches. Antiparticle beams are shaped in a damping ring and stored there until further acceleration is possible.

The next step is injecting the particles into the main accelerator. Initial acceleration is typically carried out using linear accelerators (LINACs), which consist of a sequence of individual accelerating units arranged in a straight line. However, because particles remain in the LINAC for a finite time, achieving very high energies requires long machines. To overcome this limitation, magnetic fields are used to bend the beam and guide it repeatedly through the same accelerating units, creating circular accelerators. Circular accelerators, however, also face energy thresholds: at higher energies, the beam becomes harder to bend, causing particles to exit the accelerator. Synchrotrons address this challenge by synchronizing the magnetic field with the kinetic energy of the particles, allowing for continued acceleration.

Once the desired energy levels are achieved, the beam can either be directed onto a target or collide with another beam to study high-energy interactions. Colliding beam accelerators offer a significant advantage due to their increased center-of-mass energy $\sqrt{s}$, a critical parameter in high-energy physics that determines the types of particles and interactions that can be studied. Another important parameter is the luminosity $\mathcal{L}$, which represents the proportionality between the number of interactions per second and the cross-section σ:

$$\frac{dN}{dt} = \mathcal{L}\sigma \tag{3.1}$$

At the interaction point of the beams, numerous particles are produced, but only electrons, protons, photons, and neutrinos are stable. All other particles have finite lifetimes τ and decay after traveling some distance. Depending on their lifetimes, particles such as neutrons may propagate several meters, while others decay almost immediately near the interaction point. The classification of particles involves two core tasks: detection and identification. Detection involves recognizing and counting particles, while identification involves measuring their properties, such as mass and charge. Although not all particles are charged, the detection signal typically originates from interactions of charged particles, which deposit energy in the detector components.

Charged particles deposit energy in the detector's materials, enabling their path to be tracked. In a magnetic field, the Lorentz force ($F_L \propto \vec{v} \times \vec{B}$) causes the particles to follow a curved trajectory. By analyzing this curvature within a well-calibrated magnetic field, the momentum p of the particles can be determined. Calorimeters, positioned in the detector's outer regions, measure the particles' energy. Čerenkov radiation from charged particles can also be used to identify the particle. When the particle's velocity exceeds the speed of light in a medium with refraction index n a coherent wavefront of photons is emitted. Combining all the measurements, the particle's properties, like mass and charge, can then be determined.

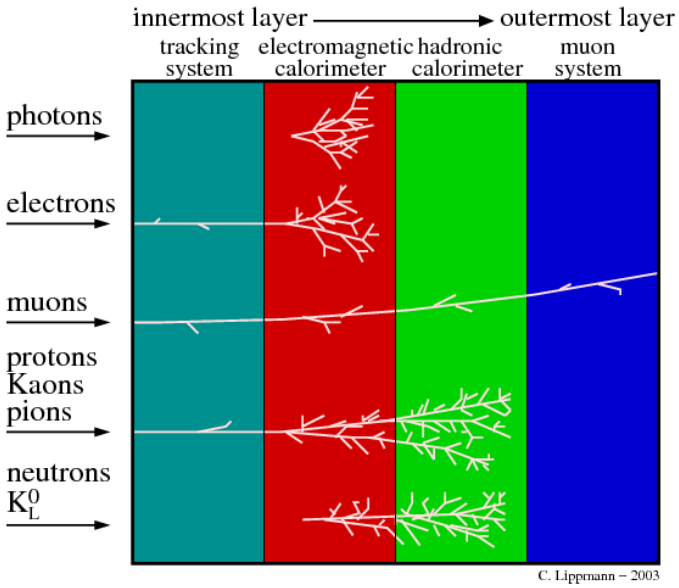

Figure 3.1: Illustration of what particles are detected and at which detector part. Image taken from [36]

Photons and high-energy electrons interact differently with detectors. For electrons, Bremsstrahlung is the most significant source of energy loss at high energies, where photons are emitted in the electrostatic field of a nucleus. Photon interactions with matter vary with energy in three ways:

1. **photoelectric effect:** the photon is absorbed by an atomic electron, which is then ejected from the atom
2. **Compton scattering:** for $E_\gamma \sim 1$ MeV the photon scatters with an electron
3. e^+e^- **pair production:** for $E_\gamma > 10$ MeV pairs of e^+e^- are created in the field of a nucleus

The photon measurement units in the detectors make use of all three effects to determine the properties of photons.

The particles produced during the collision interact at different detector parts. Photons and electrons are measured in an electromagnetic calorimeter. Muons penetrate through the whole detector and are identified by the track they leave behind in the detector. Hadrons interact with the electromagnetic calorimeter but deposit most of their energy in the hadronic calorimeter. Neutral particles like photons and neutral pions and kaons can be identified by their interactions in the calorimeter with no associated charged track. An illustration of the particles that are detected and where they deposit most of their energy in the detector is shown in Figure 3.1.

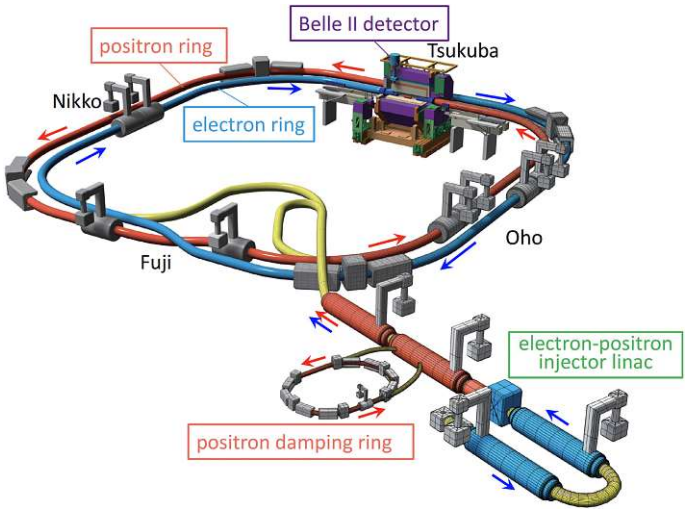

Figure 3.2: Figure illustrating the layout of SuperKEKB. The electron and positron rings consist of four linear sections identified as Tsukuba, Oho, Fuji, and Nikko. The collision between the electron and positron beams occurs precisely at the interaction point situated within the Tsukuba linear section. Image taken from [37]

3.2 SuperKEKB

The SuperKEKB collider is a significant upgrade from the KEKB B-Factory, intended to explore particle physics further and discover phenomena beyond the Standard Model.It has a design luminosity of 8×10^{35} cm^{-2}s^{-1} which is 40 times higher than its predecessor's, and aims to accumulate an integrated luminosity of 50 ab^{-1} [38]. This will be facilitated by a series of upgrades and design modifications [39]. SuperKEKB is composed of a 7 GeV electron ring (HER), a 4 GeV positron ring, the LER, which is an injector linear accelerator that includes a 1.1 GeV positron damping ring and the Belle II detector at the interaction point, as shown in figure 3.2. The center-of-mass energy corresponds to the $\Upsilon(4S)$ resonance of 10.58GeV. The strategy for upgrading revolves around optimizing beam parameters to achieve higher luminosity. Assuming flat beams and equal horizontal and vertical beam size at the interaction point, the luminosity of a collider is proportional to the total beam current I, the vertical-beam parameter ϵ_y and the vertical beta function at the interaction point β_y^*:

$$L \propto \frac{I\epsilon_y}{\beta_y^*} \tag{3.2}$$

A high luminosity is achieved by reducing beam sizes at the interaction point and doubling beam currents, which significantly enhances SuperKEKB's collision capabilities [37, 40]. The design parameters of SuperKEKB are shown in Table 3.1.

Parameter	LER	HER
Energy(GeV)	4	7
ϵ_y	0.090	0.088
β_y^* (mm)	0.27	0.41
I (A)	3.60	2.62
Luminosity ($10^{35}\text{cm}^{-2}\text{s}^{-1}$)	8	8

Table 3.1: Fundamental design parameters of SuperKEKB split up into the electron ring (HER) and the positron ring (LER) [40].

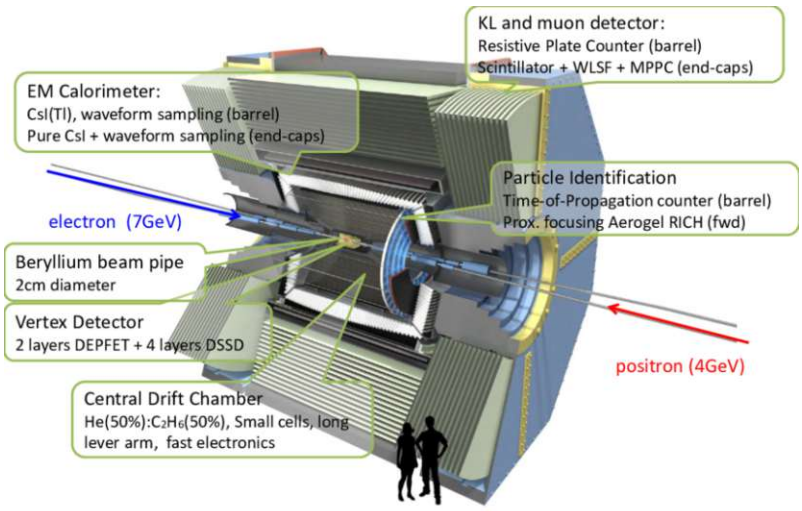

Figure 3.3: 3D view of the Belle II detector [41].

The increase in luminosity is driven by the 'nano-beam' scheme, which reduces beam size and increases currents, allowing the collider to achieve higher levels of luminosity. Modifications have been made to include new injection systems, damping rings, and redesigned interaction regions. Other upgrades include new final-focus superconducting magnets, countermeasures for electron cloud effects, and improvements to vacuum components and the RF system. The final-focus superconducting magnet system is an important element of SuperKEKB's design. It includes precise quadrupole magnets, corrector magnets, and compensation solenoid coils to achieve extremely small beta functions at the interaction point. More information about SuperKEKB can be found in references[37, 39].

3.3 Belle II Detector

The Belle II Detector has been created to function at much higher luminosities and event rates than its predecessor, Belle.

It comprises several subsystems designed to achieve a better performance in particle tracking, identification, and event reconstruction. These subsystems include the Vertex Detector (VXD), Central Drift Chamber (CDC), Particle Identification System (TOP and ARICH), Electromagnetic Calorimeter (ECL), and KL-Muon Detector (KLM). Figure 3.3 illustrates the structure of the detector and its individual subcomponents.

The VXD, comprised of the silicon Pixel Detector (PXD) and Silicon Vertex Detector (SVD) are optimized for precise vertex resolution and efficient charged particle reconstruction. The PXD has two layers of sensors, one at a radius of 14 mm and one at 22 mm, containing 8 and 12 planar sensors ("ladders") respectively. The sensors are pixelated sensors of the Depleted Field Effect Transistor (DEPFET) type. A DEPFET pixel consists of a Field Effect Transistor (FET) positioned on top of a high-resistivity, n-type, fully depleted silicon bulk. The sensors of the SVD are double-sided silicon strips.

Meanwhile, the CDC serves as a tracking device. Its large-volume drift chamber and complex wire arrangement allow for 3D helix track reconstruction. The inner cylinder has a radius of 160 mm and the outer cylinders a radius of 1130 mm. Between them are 56 layers with a total of 14336 sense wires. For the ionization gas, a mixture of He and C_2H_6 is used.

The Time-Of-Propagation (TOP) counter and Aerogel Ring Imaging Čerenkov ARICH detector, use Čerenkov radiation for particle identification. The TOP is in the barrel region of the detector and surrounds the outer cylinder of the CDC. The ARICH detector's purpose is to separate pions and kaons in a momentum range of 0.4 GeV/c to 4 GeV/c and discriminate between pions, muons, and electrons below 1 GeV/c. It is located in the forward end-cap region, which is shown in Figure 3.3 as Particle Identification.

The ECL is equipped with thallium-doped caesium iodide crystals to detect gamma rays and identify electrons. Since one-third of B decay products are neutral particles in the energy range of 20 MeV to 4 GeV, the Belle II detector relies on a high-precision electromagnetic calorimeter. It features upgraded read-out electronics to mitigate pile-up noise.

In parallel, the KLM utilizes alternating 4.7 cm thick iron plates and scintillator strips with silicon photomultipliers (SPMS) to facilitate effective muon identification while addressing background challenges. K_L mesons that do not interact in the ECL create hadronic showers that can be detected by the KLM.

The Belle II operation relies heavily on its advanced trigger system, which consists of both hardware-based low-level triggers (L1) and software-based high-level

triggers (HLT). These triggers are crucial in identifying events of interest among high background rates, allowing for efficient data acquisition and subsequent analysis. The trigger system is required to have high efficiency for $\Upsilon(4S) \to B\overline{B}$ events and from the continuum, a maximum trigger rate of 30 kHz, a latency of 5 μs, a timing precision of less than 10 ns and minimum two-event separation of 200 ns [38].

More information about the Belle II detector can be found in references [38, 40].

3.4 Other Experiments

The BaBar, CLEO, and DELPHI detectors were part of experiments conducted at e^+e^- colliders. The BaBar experiment operated at a center-of-mass energy of 10.58 GeV, corresponding to the $\Upsilon(4S)$ resonance. It was based at the Stanford Linear Accelerator Center (SLAC) Positron-Electron Project (PEP-II), an asymmetric B factory [42, 43]. In this setup, two accelerator rings were used to boost electrons to 9 GeV and positrons to 3.1 GeV.

The CLEO experiment was conducted at Cornell University in Ithaca, New York, using the Cornell Electron Storage Ring (CESR) [44, 45]. This single-ring collider facilitated symmetric collisions between electrons and positrons. Initially, data was collected at energies below the $\Upsilon(4S)$ resonance. Following system upgrades, CESR operated at resonance energies to collect data above the $B\overline{B}$ production threshold.

The DELPHI experiment focused on precision measurements of the Z boson, with a mass of $m_Z = 91.19$ GeV. To study this particle, the detector operated at center-of-mass energies above this threshold. DELPHI was one of four major detectors at the Large Electron–Positron Collider (LEP) at CERN [46].

The Collider Detector at Fermilab CDF located on the Tevatron at Fermilab was a proton-antiproton collider and the data was taken at a center-of-mass energy of $\sqrt{s} = 1.96$ TeV[47]. It is the only detector included in this thesis where experiments were conducted at $p\overline{p}$ colliders.

The key components of these detectors included:

- Silicon Vertex Tracker (SVT)/Silicon Vertex Detector (SVX): for the tracking of charged particles near the interaction point
- Drift Chamber (DHC/DR1-3): to measure the momentum and identify the particles through their energy loss
- Detector of Internally Reflected Čerenkov light (DIRC)/Ring Imaging Čerenkov (RICH) detector: to detect the Čerenkov radiation of charged particles
- Electromagnetic Calorimeter (EMC): to measure the energy of particles

- superconducting solenoid magnets: generating solenoidal magnetic fields of $1.2 - 1.5$ T
- Time Projection Chamber (TPC) and time-of-flight (TOF) detectors: for particle identification
- Instrumented Flux Return (IFR): to identify muons and neutral hadrons

3.5 Event Reconstruction

The next sections explain the reconstruction of events on the example of Belle II. Other experiments use different software and analysis tools, which can be found in references [24, 42, 46].

3.5.1 Tracking

The main information extracted from the tracking reconstruction is the momentum p of charged particles, determined from the curvature of their tracks in the magnetic field. The reconstruction process is divided into two stages: track finding and track fitting [38].

In the track finding stage, hits in the CDC and VXD corresponding to a single track are combined to form a track candidate, with pattern recognition algorithms identifying these candidates. Since the CDC and VXD are distinct detector systems, separate algorithms are employed. The VXD track finder reduces the number of track candidates by applying progressively complex filters based on the cellular automaton (CA) model [38, 48, 49]. In contrast, the CDC uses two complementary track finding algorithms: a global algorithm for initial candidate identification, which is subsequently refined by a local algorithm [38, 48].

The trajectories of the particles are then reconstructed by the track fitting system, which takes into account the energy loss, multiple scattering in detector materials, and variations in the magnetic field. The deterministic annealing filter (DAF) is the primary track fitting algorithm in Belle II, built on the Kalman filter (KF) and implemented through the `GENFIT` package [38, 50, 51, 52, 53].

3.5.2 Charged Particle Identification

Effective charged particle identification (PID) is essential for isolating hadronic final states, reducing background noise, and enabling flavor-tagging techniques [38]. The PID system combines measurements from the TOP and ARICH detectors, along with dE/dx measurements from the CDC and VXD, to construct a combined likelihood ratio, which is used to identify particles [38].

3.5.3 Neutral particle identification

Photons are identified by the shower shape of ECL clusters that do not match a reconstructed track. The shower shape itself is considered, as photon showers are cylindrically symmetric in the lateral direction. In contrast, surrounding energy deposits from beam background—such as neutral and charged hadrons—produce asymmetric shower shapes involving multiple ECL clusters [38].

The π^0 is reconstructed from the decay $\pi^0 \to \gamma\gamma$. Depending on the energies of the π^0 different criteria are used to identify the particle. For energies below 1 GeV, the photons produce two non-overlapping ECL clusters. In the energy range of 1 GeV to 2.5 GeV, overlapping clusters are produced, but the individual photons can still be reconstructed. For energies above 2.5 GeV, separate local maxima are no longer distinguishable, and the photon pair is reconstructed as a single cluster [38].

3.6 Monte Carlo Simulations

Monte Carlo (MC) simulations are fundamental tools in high-energy physics experiments, serving multiple purposes in experimental design, data analysis, and interpretation. One of the primary uses of MC simulations in collider experiments is modeling how particles interact with the detectors. Particles produced during collision pass through various layers of the detector, each designed to measure different properties. MC simulations replicate these interactions by incorporating detailed descriptions of the detector geometry and materials. This allows for predictions of how particles should behave in the detector, which is important for understanding the efficiency and resolution of the measurement apparatus. Belle II uses a simulation package for particle interactions with detector material based on `Geant4` [54, 55].

A major challenge in high-energy physics is distinguishing rare signal events from overwhelming background noise. MC techniques are used to simulate known background processes, providing a model of their contributions. By comparing simulated background distributions with experimental data, background events can be estimated and subtracted from the data, to improve the signal extraction. The background continuum processes $e^+e^- \to q\bar{q}$ for Belle II are simulated with `KKMC` and `PYTHIA` [56, 57].

MC simulations also generate theoretical predictions for specific signal processes that are studied. These simulated B meson decays are crucial for validating theoretical models and for developing event selection criteria that optimize signal detection while suppressing background events. Simulated datasets serve as essential references for analyzing real experimental data. The main event generator for Belle II is `EvtGen` [58]. The same reconstruction and analysis algorithms applied to exper-

imental data are also used for simulated events. This consistency facilitates the development and optimization of selection criteria and fitting procedures, ensuring that biases are minimized and that statistical interpretations are robust. All the simulation modules and analysis tools of Belle II are packed together in the `basf2` software [59].

Chapter 4

Data Analysis and Reconstruction of $B \to X_c l \nu$

This chapter provides an overview of data analysis and reconstruction of events in collider experiments, using Belle II as an example, and explains how moments of inclusive $B \to X_c l \nu$ are measured. Section 4.1 presents the reconstruction of B decays, with a focus on inclusive decays. The reconstruction and selection for the B mesons are explained in Sections 4.2 and 4.3. The measurement of the moments is explained using the example of the leptonic invariant mass spectrum q^2 in Section 4.4. Finally, Section 4.5 introduces the observables used in the fit, including the definition of the moments and the corresponding experimental data.

4.1 Decay Reconstruction

Studying the properties of B mesons is challenging because they decay near the interaction point. Therefore, their reconstruction relies on identifying the final-state particles. These final-state particles may originate directly from a B decay, such as $B^0 \to K^+K^-$, or be produced through a decay chain, for example:

$$\begin{aligned} B^0 \to & D^{*-}\pi^+\pi^0 \\ & \pi^0 \to \gamma\gamma \\ & D^{*-} \to D^0\pi^- \\ & \quad D^0 \to K^+\pi^- \end{aligned} \tag{4.1}$$

Exclusive decays, or fully hadronic decays, are reconstructed from the four-momenta of their final-state particles. A full reconstruction of (semi-) leptonic decays is not possible, because the neutrinos are not measured and leave the detector undetected [24]. The decay chain is started to be reconstructed at the final-state

particles. In the example above, K^+ and π^- form a D^0; D^{*-} are formed by combining D^0 with π^-; two photons are combined to form a π^0; and in the final step D^{*-}, π^+ and π^0 are combined to a B^0. At each stage, the four-momentum is obtained by summing the four-momenta of the decaying particles, according to the law of momentum conservation [24].

In some cases, particles used to reconstruct a parent particle may be incorrectly identified and are called background events. Random combinations of particles that are not produced in the specific decay are called combinatorial background [24]. Final-state particles can originate from different decays, or multiple particles may trace back to a single decay. For example, the π^+ and the D^{*-} in the decay $B^0 \to D^{*-}\pi^+\pi^0$ can originate from different B decays. Another significant contribution to the combinatorial background arises from continuum events. In these events, instead of a B meson pair, a lighter meson is produced and is usually the dominant background in rare B decays [24].

Another source for background events are misidentified final-state particles, which contribute to the so-called physics background. Additionally, many decays lead to the same final-state particles, resulting in ambiguities where events may be incorrectly attributed to the wrong decay.

4.1.1 Reconstruction of $B \to X_c l\nu$

Semileptonic decays are characterized by the presence of a lepton-neutrino pair. This makes the study of such decays challenging, as the neutrino is undetectable, preventing full reconstruction of the decay. To gather information and apply constraints to a decay, both B mesons from the $\Upsilon(4S)$ decay are reconstructed. Information from one reconstructed B meson, together with the precisely known initial state, constrain the other B meson. If one decay is fully reconstructed, all remaining tracks and energy depositions in the detector must therefore originate from the other B, referred to as "signal-side" B (B_{sig}) [24, 38, 42]. The fully reconstructed B is called "tag-side" B (B_{tag}). An illustration of the tag-side and signal-side is shown in Figure 4.1, where ROE stands for Rest-Of-Event and includes any hadronic decay.

The $\Upsilon(4S)$, with an energy of 10.58 GeV, lies just above the production threshold for $B\overline{B}$ pair production, as shown in Figure 2.4. In the center-of-mass (CM) frame the B_{tag} and B_{sig} mesons are produced almost at rest, which can be expressed through four-momentum conservation:

$$p^*_{B_{tag}} + p^*_{B_{sig}} = 0 \tag{4.2}$$

If the B_{sig} is reconstructed in a semileptonic decay and the B_{tag} in a fully hadronic decay, the neutrino's momentum can be determined from the four-momentum conservation in equation 4.2. This provides a kinematic constraint on the missing mass

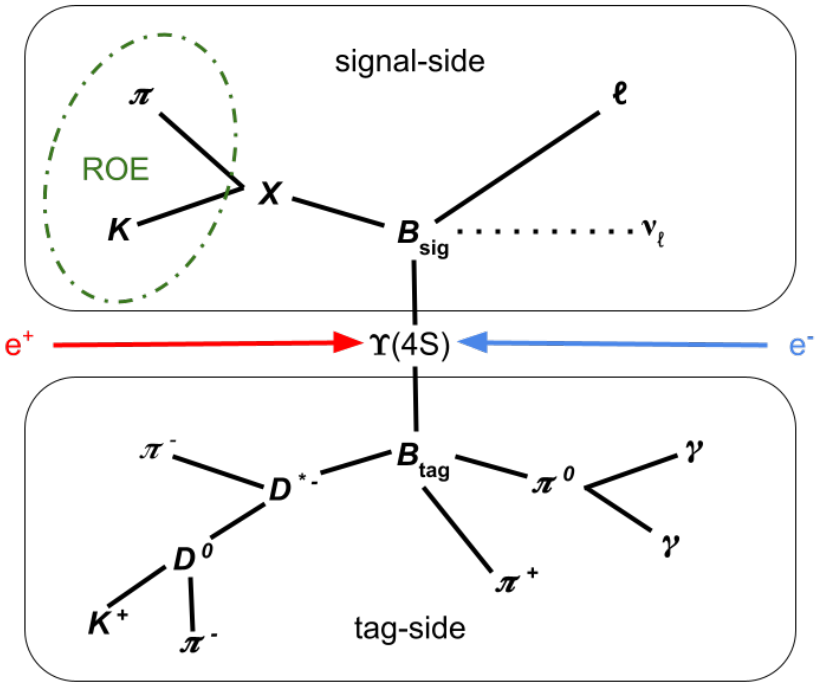

Figure 4.1: Illustration of an $\Upsilon(4S) \rightarrow B\overline{B}$, with the B_{sig} in a semileptonic decay and B_{tag} in a fully hadronic decay.

squared, which peaks at the neutrino mass of zero for correctly reconstructed events [24].

This approach is applied to inclusive semileptonic decays. The B_{tag} is fully reconstructed through a hadronic decay, while the B_{sig} is identified by a lepton. Any leftover charged particle tracks and ECL clusters that were not utilized in the reconstruction of the signal lepton l and the B_{tag}, can be attributed to the hadronic system X.

Two key variables are used when constraining the tag-side: the beam-constrained mass m_{bc} and the energy difference ΔE. The beam-constrained mass is given by

$$m_{bc} = \sqrt{(E^*_{beam})^2 - (\vec{p_B}^*)^2}, \tag{4.3}$$

and the energy difference ΔE is defined as

$$\Delta E = E^*_B - E^*_{beam}. \tag{4.4}$$

The signal of m_{bc} peaks at the B meson mass m_B and it depends only on the momenta of the daughter particles, not on their assumed mass. The resolution in m_{bc} is determined by the spread in the energy of the colliding beams [24]. The expected value of ΔE for correctly reconstructed decays is zero and depends on the assumed masses of the particles used in the reconstruction. The resolution for ΔE is dominated by the detector resolution [24].

The next sections explain the tag- and signal-side reconstruction, and the measurements of moments in $B \to X_c l \overline{\nu}_l$ on the example of the q^2 moments measured at Belle II [60]. Other analyses apply different methods of reconstruction, depending on the experiment and the measured moment.

4.2 Tag-Side Reconstruction and Selection

Belle II uses the Full Event Interpretation (FEI) algorithm to reconstruct B_{tag} candidates in fully hadronic decays [61]. The reconstruction starts by selecting charged and neutral final-state particles (illustrated in Figure 3.1) from tracks and ECL clusters. They are then combined into intermediate particles, which are subsequently used to form B_{tag} candidates. The FEI utilizes an optimized stochastic gradient-boosted decision tree implementation to determine the signal probability $\mathcal{P}_{FEI}$, which quantifies the likelihood that each candidate in a decay chain is correctly reconstructed [62]. Kinematic and vertex fit information, combined with the signal probability of the previous stages, is used to reconstruct more than 100 explicit decays, leading in $\mathcal{O}(10,000)$ decay chains [61].

In reference [60] they selected events with at least three charged particles and three ECL clusters to suppress continuum processes. Additionally, the ratio of the second and zeroth Fox-Wolfram moments R_2 has to be smaller than 0.4 and $cos(\theta_T) < 0.7$, to reduce the continuum background. Here, θ_T represents the angle between the thrust axis of the B_{tag} decay products and the thrust axis of the remaining event. The total energy in the ECL is constrained by $2\,\text{GeV} < E_{ECL} < 7\,\text{GeV}$ and the total visible energy is required to be greater than 4 GeV. The B_{tag} candidates are selected by requiring $\mathcal{P}_{FEI} > 0.01$, $M_{bc} > 5.27 GeV$, and $-0.15\,\text{GeV} < \Delta E < 0.1\,\text{GeV}$.

Measurements at other experiments do not use the FEI algorithm. In references [63, 64], which measure the hadronic invariant mass and lepton energy spectrum at Belle, the specific decay modes $B^+ \to \overline{D}^{(*)0}\pi^+$, $\overline{D}^{(*)0}\rho^+$, $\overline{D}^{(*)0}a_1^+$, $B^0 \to D^{(*)-}\pi^+$, $D^{(*)-}\rho^+$, $D^{(*)-}a_1^+$, as well as their charge-conjugated decay, together with their subdecays to kaons and pions are used to reconstruct the B_{tag} candidates. Constraints on the final-state and intermediate particles (photon energy E_γ, K_S^0 invariant mass, ...) are used to suppress the continuum background. A final distribution of m_{bc} for B^0 and B^+ candidates is shown in Figure 4.2, with the peaks at the B masses.

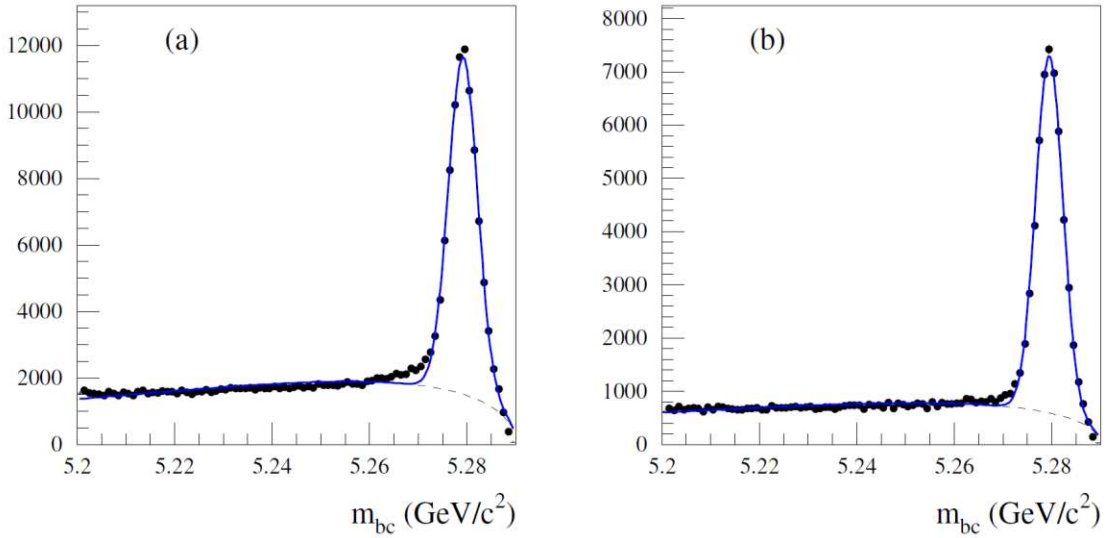

Figure 4.2: M_{bc} distributions in real data for fully-reconstructed (a) B^+ and (b) B^0 decays. The background is fitted with an Argus function and the signal with a Gaussian function. The image is taken from reference [70].

The data analysis of hadronic moments at BaBar [65] also uses the full hadronic reconstruction of B_{tag} to constrain B_{sig}. The measurement of the lepton energy spectrum at BaBar uses a different kind of approach by tagging electrons e_{tag} [66]. At CDF, CLEO, and DELPHI the semileptonic B_{sig} decay is directly reconstructed without the use of B_{tag} [67, 68, 69].

4.3 Signal-side Reconstruction and Selection

The signal-side B decays are identified by their leptons. In reference [60], the following constraints on the decay reduce the background: laboratory frame momenta $p_{lab} > 0.5\,\text{GeV}$; distances of closest approach to the interaction point IP $d_r < 1\,\text{cm}$ and $|d_z| < 2\,\text{cm}$; at least one hit in the CDC and polar angle within $[17°, 150°]$; $\mathcal{P}_l = \mathcal{L}_l/(\mathcal{L}_e + \mathcal{L}_\mu + \mathcal{L}_\pi + \mathcal{L}_K + \mathcal{L}_p + \mathcal{L}_D) > 0.9$. The four-momenta of photons lost to Bremsstrahlung are added to the four-momenta of electrons. Similar constraints, especially on momentum and polar angle, are utilized in the measurements of the other moments.

Particles with low-momentum can loop within the CDC and may be reconstructed as multiple tracks. These tracks are identified with the transverse momenta $p_t < 275\,\text{MeV}$ and the track with the smallest value of $(5d_r)^2 + |d_z|^2$ is selected. The remaining charged tracks and neutral clusters identify the X_c system, which is not explicitly reconstructed.

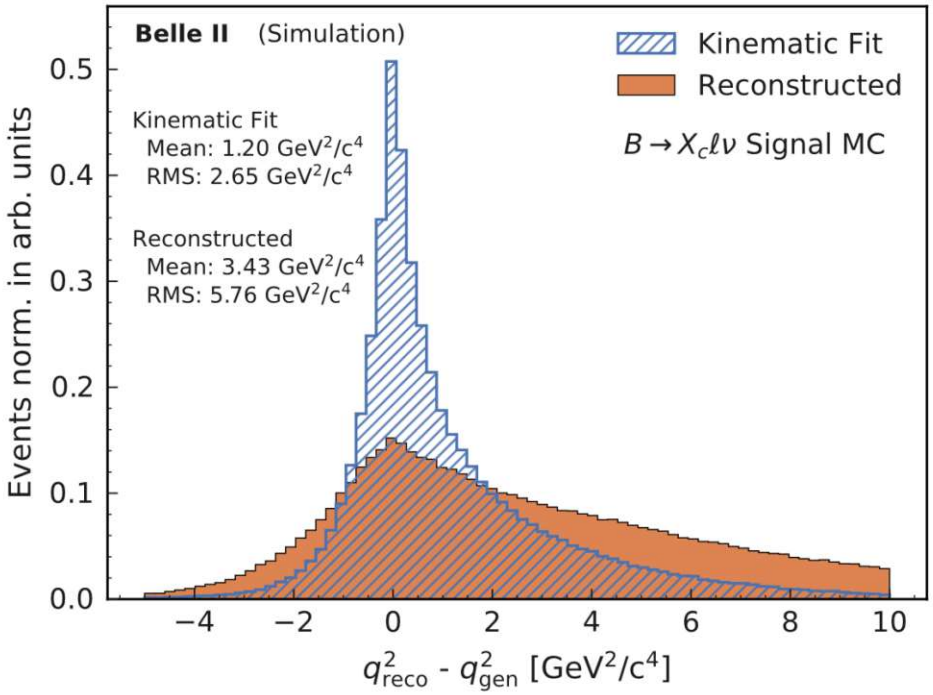

Figure 4.3: Comparison of q^2 for $B \to X_c l\overline{\nu}_l$ reconstructed ('reco') and generated ('gen') data. Image taken from reference [60].

The four-momentum missing from the event should be only due to the neutrino. It is reconstructed as

$$p_{miss} = p_{e^+e^-} - p_{B_{tag}} - p_X - p_l. \tag{4.5}$$

Here, $p_{e^+e^-}$ is the four-momenta of the colliding beams. The constraints of reference [60] $E_{miss} > 0,5\,\text{GeV}$ and $|\boldsymbol{p}_{miss}| > 0.5\,\text{GeV}$ improve the resolution on the mass of X_c system m_X. All other measurements also use some kind of constraint on the missing momentum.

For q^2, additional kinematic fits are employed to improve the resolution [60]. In Figure 4.3, a comparison of q^2 distributions before and after the kinematic fit is shown. The fit minimizes the following χ^2 function

$$\chi^2 = \sum_{i\in\{B_{tag},X,l\}} (\hat{p}_i - p_i) C_i^{-1} (\hat{p}_i - p_i), \tag{4.6}$$

where $\hat{p}_i$ is the fitted four-momentum and C_i is the covariance matrix. The fitted four-momenta are then constrained by: $\hat{p}_X^2 > 0\,\text{GeV}^2$; $\hat{p}_{B_{tag}}^2 = m_B^2$; $(\hat{p}_l + \hat{p}_X + \hat{p}_\nu)^2 = m_B^2$; $(\hat{p}_{e^+e^-} - \hat{p}_{B_{tag}} - \hat{p}_l - \hat{p}_X - \hat{p}_\nu) = 0$.

4.4 Measurement of Moments in $B \to X_c l \overline{\nu}_l$ Decays

Before the mean of the moments can be calculated, contributions from background events need to be subtracted by applying binned likelihood fits to the m_X^2 distribution to receive the number of signal and background events. Background events are considered from the following two sources: $e^+e^- \to q\overline{q}$ continuum events ($n_{q\overline{q}}$) and $B\overline{B}$ background events from secondary leptons and misidentified signal leptons ($n_{B\overline{B}}$). The shape of these backgrounds is determined from MC simulation and fit to the real data.

The background of q^2 from other processes is removed through an unbinned method that utilizes event weights, based on the reconstructed hadronic mass spectrum m_X^2. An event-wise signal probability $w_i(q^2)$ is computed for a given q^2, which gives the probability that an event in bin i is a signal event. The continuous signal probability $w(q^2)$ is obtained by cubic spline interpolation of the $w_i(q^2)$. The background-subtracted weighted q^2 mean of order n is given by

$$\langle q^{2n} \rangle = \frac{\sum_i^{N_{data}} w(q_i^2) \times q_{calib,i}^{2n}}{\sum_j^{N_{data}} w(q_j^2)} \times \mathcal{C}_{calib} \times \mathcal{C}_{gen}. \tag{4.7}$$

Here, the sums go over all events and q_{calib}^2 indicates the reconstructed q^2 corrected for acceptance and reconstruction effects. The calibration factor $\mathcal{C}_{calib}$ is introduced to correct the bias of the calibration of the q_{calib}^2 and the factor $\mathcal{C}_{gen}$ accounts for the bias of the B_{tag} reconstruction and Belle II detector acceptance.

The measurements at BaBar follow a similar procedure as for the q^2 moments and are calculated with equation 4.7 adapted to the BaBar detector and for E_l or m_X^2 moments [65, 66].

For the Belle E_l and m_X^2 moments [64, 63], the measured distributions are corrected for the distortions from the detector. To get the true spectrum, the measured distributions are unfolded using the Singular Value Decomposition (SVD) algorithm [71]. The detector effects are obtained from MC simulation and depend on the physics model and detector response. The effects of unfolding a m_X^2 distribution are shown in Figure 4.4. The mean value for a first moment M can then be calculated with

$$\langle M \rangle = \frac{\sum_i M_i x_i'}{\sum_i x_i'}, \tag{4.8}$$

where x_i' is the unfolded spectrum.

The measurements at CDF, CLEO, and DELPHI [67, 68, 69], combine the individual branching fractions and measured moments to get an averaged moment with a formula like

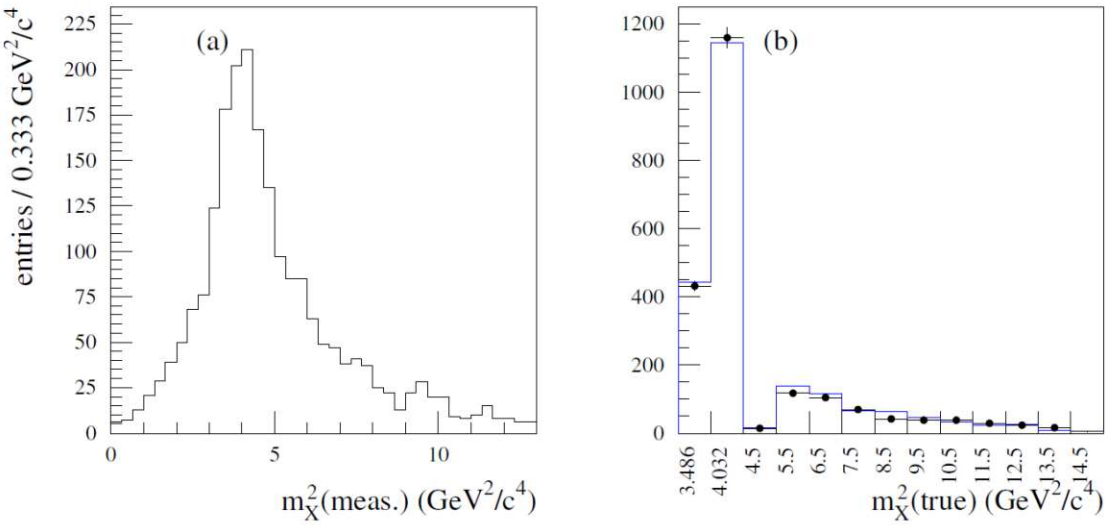

Figure 4.4: Measured (a) and true (b) m_X^2 distributions of MC simulation. The spectrum in (a) is obtained by applying the detector simulation to the true m_X^2 data (blue histogram) in (b). The data points in (b) are computed by using the SVD algorithm on the measured distribution. Data taken from reference [63].

$$\langle M \rangle = \frac{\sum_i BR_i M_i}{\sum_i BR_i}, \tag{4.9}$$

where BR_i are the branching fractions of the mode i, and M_i are the measured moments. Different corrections and terms are included depending on the experiment. More detail on the exact extraction of the moments can be found in references [67, 68, 69].

4.5 Observables Included in the Fit and Data Selection

For the extraction of $|V_{cb}|$ from inclusive semileptonic decays, theoretical predictions are fitted to experimental data. These theoretical computations depend on the HQE parameters, which are also determined through the fit. To extract the HQE parameters reliably, it is essential to achieve a good convergence of the theoretical formula in both α_s and $1/m_b$, while ensuring that the observable is experimentally precisely measurable. The observable should be sensitive to the HQE parameters, but the deviation from tree-level predictions should be minimal so that the contributions from higher-dimension operators in the OPE are not too dominant [72]. Further-

more, the observable should not depend on $|V_{cb}|$, as it is the key parameter in this analysis. The Observables best suited for the OPE are the hadronic invariant mass spectrum m_X^2 and lepton energy distribution E_l, as suggested by references [72] and [73].

The normalized moments are defined as the leptonic energy distribution

$$\langle E_l^n \rangle_{E_l > E_{cut}} = \frac{\int_{E_{cut}}^{E_{max}} E_l^n \frac{d\Gamma}{dE_l} dE_l}{\int_{E_{cut}}^{E_{max}} \frac{d\Gamma}{dE_l} dE_l}; \tag{4.10}$$

the hadronic invariant mass distribution

$$\langle m_X^{2n} \rangle_{E_l > E_{cut}} = \frac{\int_{E_{cut}}^{E_{max}} m_X^{2n} \frac{d\Gamma}{dm_X^2} dm_X^2}{\int_{E_{cut}}^{E_{max}} \frac{d\Gamma}{dm_X^2} dm_X^2}. \tag{4.11}$$

The lepton energy is constrained with a lower limit $E_l \geq E_{cut}$ to reduce background events and the moments are measured for different values of E_{cut}. Since the OPE is dependent on the value of E_{cut}, this provides additional information for the fit. Another observable, the ratio R^*, is introduced to relate the actual measured rate with the total rate. The ratio R^* is defined as:

$$R^*(E_{cut}) = \frac{\int_{E_{cut}}^{E_{max}} dE_l \frac{d\Gamma}{dE_l}}{\int_0^{E_{max}} dE_l \frac{d\Gamma}{dE_l}} \tag{4.12}$$

An alternate method to using E_l and m_X^2 has been proposed by reference [8] with a reduced set of higher-dimension operators. The methods in reference [8] rely on the Reparametrization Invariance (RPI), which changes the definitions of HQE parameters [74]. The normalized q^2 moments are defined as

$$\langle q^{2n} \rangle = \frac{m_b^{2n} \int_{q^2_{cut}}^{q^2_{max}} q^{2n} \frac{d\Gamma}{dq^2} dq^2}{\int_{q^2_{cut}}^{q^2_{max}} \frac{d\Gamma}{dq^2} dq^2}. \tag{4.13}$$

Here, instead of lower cuts on E_l, the moments are computed with lower constrain for the leptonic invariant mass. The q^2 moments are measured at different values for q^2_{cut} and provide more information for the fit.

This thesis does not employ the RPI approach in reference [8], but instead uses the calculations of reference [10], which uses the same set of operators as the calculations for the E_l & m_X^2 moments.

The moments with $n = 1, 2, 3$ in equations 4.10 and 4.11 are highly correlated. The physical information extracted from them does not provide significant new information, so it is more effective to use the central moments. The central moments with the subscript 1 are the mean of the distribution, the ones with 2 are the squared

deviation from the mean, also called the variance, and the subscript 3 is used for the asymmetry of the distribution. They are defined as

$$l_1 = \langle E_L \rangle, \qquad l_2 = \langle (E_l - \langle E_l \rangle)^2 \rangle, \qquad l_3 = \langle (E_l - \langle E_l \rangle)^3 \rangle, \tag{4.14}$$

for the lepton energy,

$$h_1 = \langle m_X^2 \rangle, \qquad h_2 = \langle (m_X^2 - \langle m_X^2 \rangle)^2 \rangle, \qquad h_3 = \langle (m_X^2 - \langle m_X^2 \rangle)^3 \rangle, \tag{4.15}$$

for the invariant hadronic mass, and

$$Q_1 = \langle q^2 \rangle, \qquad Q_2 = \langle (q^2 - \langle q^2 \rangle)^2 \rangle, \qquad Q_3 = \langle (q^2 - \langle q^2 \rangle)^3 \rangle, \tag{4.16}$$

for the leptonic invariant mass.

The experimental data for the global fit on E_l and m_X^2 moments were collected from BaBar, Belle, CLEO, CDF, and DELPHI. A total of 50 measurements were used. Table 4.1 shows the moments used, with their corresponding E_{cut} values, and the experiments from which they were taken. For $E_{cut} > 1.5\,\text{Gev}$ the expansion in inverse powers of the bottom quark mass $1/m_b$ becomes unreliable [75]. The higher-order non-perturbative effects become more important with increasing E_{cut} and so only measurements with a value of $E_{cut} \leq 1.5\,\text{GeV}$ are chosen for the fit, even if measurements with higher cut value were available.

An overview of the experimental data used for the fits on q^2 moments is shown in Table 4.2. A total of 27 measurements from Belle and Belle II were included, each corresponding to different values of q^2_{cut}. The Belle measurements consist solely of data for electrons, while for the Belle II data, an average of both electron and muon data was used. A breakdown of the OPE can be observed at higher values of q^2_{cut}, similar to higher E_{cut} values for hadronic invariant mass and lepton energy spectrums. In reference [10] it is shown that for $q^2_{cut} > 8\,\text{GeV}$ higher-order corrections become relevant, which were not included in the calculations. To avoid this problem, only measurements with a value of $q^2_{cut} < 8\,\text{GeV}$ were used in this thesis.

Because the measured moments exhibit a high level of correlation, this thesis does not examine the complete set of moments from each experiment. Instead, only the subsets in Tables 4.1 and 4.2 are used. It is important to emphasize that the analysis outcome remains largely unaffected by the specific subset selected and that they are consistent with the experimental data used in references [6, 7, 9, 10].

Observable	E_{cut} (GeV) values	Ref.	Experiment
R^*	0.6, 1.2, 1.5	[65, 66]	BaBar
l_1	0.6,0.8,1, 1.2, 1.5	[65, 66]	BaBar
l_2	0.6, 1, 1.5	[65, 66]	BaBar
l_3	0.8, 1.2	[65, 66]	BaBar
h_1	0.9, 1.1, 1.3, 1.5	[65]	BaBar
h_2	0.8, 1, 1.2, 1.4	[65]	BaBar
h_3	0.9, 1.3	[65]	BaBar
R^*	0.6, 1.4	[64]	Belle
l_1	1, 1.4	[64]	Belle
l_2	0.6, 1.4	[64]	Belle
l_3	0.8, 1.2	[64]	Belle
h_1	0.7, 1.1, 1.3, 1.5	[63]	Belle
h_2	0.7, 0.9, 1.3	[63]	Belle
$h_{1,2}$	0.7	[67]	CDF
$h_{1,2}$	1, 1.5	[68]	CLEO
$l_{1,2,3}$	0	[69]	DELPHI
$h_{1,2,3}$	0	[69]	DELPHI

Table 4.1: Experimental data used in fits on hadronic and leptonic data.

Observable	q^2_{cut} (GeV) values	Ref.	Experiment
Q_1	3.0, 4.5, 6.0, 7.5	[76]	Belle
Q_2	3.0, 4.5, 6.0, 7.5	[76]	Belle
Q_3	3.0, 4.5, 6.0, 7.5	[76]	Belle
Q_1	1.5, 3.0, 4.5, 6.0, 7.5	[60]	Belle II
Q_2	1.5, 3.0, 4.5, 6.0, 7.5	[60]	Belle II
Q_3	1.5, 3.0, 4.5, 6.0, 7.5	[60]	Belle II

Table 4.2: Experimental data used in fits on q^2 moments.

Chapter 5

Semileptonic Global Fit

This chapter provides an overview of how the fits on moments from semileptonic inclusive decays are performed. The computation of the theoretical errors and correlation is discussed in section 5.2. Section 5.3 focuses on the external constraints applied to the fit. Parameters and physical constants, calculated by different groups, are included to ensure the convergence of the fit. Finally, section 5.4 explains the fit procedure and the definition of the χ^2 function. At the end of the chapter, some corrections to the theoretical computation and experimental measurements of the moments that were calculated since the publication of the original papers are introduced.

5.1 Computations of Moments in Semileptonic Decays

The inclusive extraction of $|V_{cb}|$ from a fit requires a computation of the individual moments. With the HQE theory and OPE (see Sections 2.5 and 2.4) the moments are expanded in orders of $1/m_b$. The total expansion is expressed in non-perturbative matrix elements and perturbative Wilson coefficients. At each order of $1/m_b$, the Wilson coefficients are expanded in α_s, as they encapsulate the short-distance effects. The two matrix elements at order $1/m_b^2$ are identified with μ_π^2 and μ_G^2. At order $1/m_b^3$ the two matrix elements are ρ_D^3 and ρ_{LS}^3.

The codes compute the moments at a given value of E_{cut} (for E_l and m_X^2 moments) or q_{cut}^2 (for q^2 moments) and take as input the HQE parameters μ_π^2, ρ_D^3, μ_G^2, ρ_{LS}^3, as well as the heavy quark masses m_b and m_c. The computation of the total semileptonic width requires two additional parameters: the semileptonic branching ratio $BR_{cl\nu}$ and the CKM parameter $|V_{cb}|$. Eight total parameters are not determined by the computations and are obtained from a fit on real data.

Computations of E_l and m_X^2 moments

The code for the computations of the E_l and m_X^2 moments was provided from reference [77, 6]. The code evaluates the perturbative corrections to the moments up to α_s^2 at order $\mathcal{O}(1)$, α_s/m_b^2 at order $\mathcal{O}(1/m_b^2)$ and includes $\mathcal{O}(1/m_b^3)$ corrections. In Table 5.1 the perturbative corrections are summarized. The specific references for the corrections can be found in [77, 6].

$\langle E_l^n; (m_X^2)^n \rangle$	tree	α_s	α_s^2	α_s^3
Partonic	✓	✓	✓	
μ_π^2	✓	✓		
μ_G^2	✓	✓		
ρ_D^3	✓			
ρ_{LS}^3	✓			

Table 5.1: Overview of the perturbative corrections available for the E_l and m_X^2 moments. The checkmarks indicate the corrections that are used in the code from references [77, 6].

Computations of semileptonic width Γ_{sl}

The semileptonic width is computed to determine $|V_{cb}|$. The code for the calculation comes from reference [7] and incorporates the α_s^3 and $\alpha_s\rho_D^3/m_b^3$ corrections. The used perturbative corrections are shown in Table 5.2. The specific references for the corrections can be found in [7].

$\langle\Gamma_{sl}\rangle$	tree	α_s	α_s^2	α_s^3
Partonic	✓	✓	✓	✓
μ_π^2	✓	✓		
μ_G^2	✓	✓		
ρ_D^3	✓	✓		
ρ_{LS}^3	✓			

Table 5.2: Overview of the perturbative corrections available for the total semileptonic width Γ_{sl}. The checkmarks indicate the corrections that are used in the code from reference [7].

Computations of q^2 moments

The code for the computations of the q^2 moments was provided from reference [10]. The code evaluates the perturbative corrections to the moments up to α_s^2 at order $\mathcal{O}(1)$, α_s/m_b^2 at order $\mathcal{O}(1/m_b^2)$ and α_s/m_b^3 at order $\mathcal{O}(1/m_b^3)$. In Table 5.3 the perturbative corrections are summarized. The specific references for the corrections can be found in [10].

$\langle(q^2)^n\rangle$	tree	α_s	α_s^2	α_s^3
Partonic	✓	✓	✓	
μ_π^2	✓	✓		
μ_G^2	✓	✓		
ρ_D^3	✓	✓		
ρ_{LS}^3	✓	✓		

Table 5.3: Overview of the perturbative corrections available for the lepton invariant mass q^2. The checkmarks indicate the corrections that are used in the code from reference [10].

5.2 Theory Errors and Correlations

The theoretical calculations of the moments are subject to several sources of uncertainty. First, there are terms that are intrinsically beyond the OPE and are not considered in this thesis. Another source of uncertainty arises from missing higher-order terms. In equation 2.28, the series extends infinitely, but for practical calculations, it is truncated at $1/m_b^3$. The contributions from these higher-order terms are estimated and incorporated into the uncertainty of the theoretical predictions.

5.2.1 Theory Errors

In this thesis, the theory errors are estimated by varying the input parameters used in the calculation of the moments. The calculation of the theoretical error is carried out according to the following steps. First, the moments are evaluated for each parameter individually shifted with the codes presented in Section 5.1. The squared differences between the shifted and unshifted values are then summed. To obtain the final theoretical error, the square root of the sum is taken and multiplied by 1/2, as the parameters are varied to lower and higher values. This method of computing the theory error is applied to all moments: E_l, m_X^2 and q^2.

The masses of the bottom and charm quark are varied by 4 MeV. The shift for the HQE parameters, μ_π^2 and μ_G^2, are set to 7 %. The shift of the other HQE parameters, ρ_D^3 and ρ_{LS}^3, is set to 20 %. Finally, α_s is varied by ± 0.018. These variations follow the suggestions in references [6, 7] and are also implemented in reference [10].

5.2.2 Theory Correlations of Leptonic and Hadronic Moments

Estimating the theory correlations between leptonic E_l and hadronic m_X^2 moments is more challenging than determining their theoretical errors. In general, there is no reason why two different moments, such as l_1 and h_2, should be correlated with each other. Known correlations also show no clear pattern and therefore different moments are considered as uncorrelated [78]. However, further examination of the calculations reveals some interesting observations. When l_1 and h_2 receive a negative contribution from varying ρ_D^3 by $\pm 20\%$, a positive correlation between the two moments is observed. The aim of estimating the theoretical correlations is not to compute them exactly but to provide an approximation. Therefore, the safest approach is to disregard the observed correlations when making theoretical predictions for different moments [78].

However, correlations for the same moment at different values of E_{cut} cannot be ignored. Evaluating a moment M_i at two values of E_{cut}, say E_1 and E_2, that are

close to each other will result in OPEs that are nearly identical. This leads to a very high correlation for the moments $M_i(E_1)$ and $M_i(E_2)$. This observation is supported by the study of the $1/m_b^{4,5}$ contribution, where it was found that for values of E_{cut} below 1.2 GeV, the contributions are nearly equal and thus highly correlated [31]. When the difference between the two values $|E_1 - E_2|$ increases, the correlation is expected to decrease, as the OPEs will differ more from each other.

The theoretical correlation model used in this thesis is based on scenario **D** in reference [78]. The correlation ξ is fixed for a moment M_i computed at E_{cut} and $E_{cut} + 0.1\text{GeV}$. The scaling factor ξ depends on E_{cut} and is defined as:

$$\xi(E_{cut}) = 1 - \frac{1}{2} e^{-\frac{E_0 - E_{cut}}{\Delta}} \tag{5.1}$$

Here, $E_0 \approx 1.75(GeV)$ is the partonic endpoint and the adjustable parameter Δ is set to 0.25GeV. The factor ξ is close to 1 for lower cuts and drops for values of E_{cut} higher than 1.2GeV.

The theoretical correlations are calculated with a toy MC simulation. The computed moments are randomly varied in their calculated error for a total of 10,000 iterations. The correlation for moments M_i and M_j is then calculated with the following standard formula:

$$cor_{i,j} = \frac{E[(M_i - \mu_i)(M_j - \mu_j)]}{\sqrt{E(M_i^2) - E(M_i)^2}\sqrt{E(M_j^2) - E(M_j)^2}}, \tag{5.2}$$

where $\mu_{i,j}$ is the value of the moment with unvaried HQE parameters, and $M_{i,j}$ are the values generated by the MC.

The values $cor_{i,j}$ are then multiplied by $\xi(E_{cut})$ from equation 5.1 for each 0.1 GeV step between $E_{i,cut}$ and $E_{j,cut}$. For the starting value of E_{cut} in equation 5.1, the lower value of $E_{i,cut}$ and $E_{j,cut}$ plus an offset of 0.05 GeV is chosen. For example, the total scaling factor of the cuts 0.8 GeV and 1.2 GeV is $\prod_{k=0}^{k=3} \xi(0.85 + 0.1 \times k\,\text{GeV}) \approx 0.89$.

5.2.3 Theory Correlations of q^2 moments

The computation of the theoretical correlation of the q^2 moments follows a similar approach to that used for the E_l & m_X^2 moments. The methods of option **D** in reference [78] were adopted to the q^2 moments [10].

Different central moments are considered uncorrelated, and the same moments at different cuts on q^2 are scaled with a factor $\xi(q^2_{cut})$ [10]. The factor is defined as

$$\xi(q^2_{cut}) = 1 - \frac{1}{2} e^{-\frac{q_0^2 - q^2_{cut}}{\Delta_q}}, \tag{5.3}$$

where the parameters q_0^2 and Δ_q are chosen so that the correlation between cuts far from each other and near the endpoint remains small. Moments with cuts close

to each other and at lower q^2 values should have a high correlation. In this thesis, the parameters are $q_0^2 = 9\,\mathrm{GeV}^2$ and $\Delta_q = 1.4\,\mathrm{GeV}^2$, as suggested by reference [10].

The correlations are computed with the same steps as before. First, the theoretical error is determined by varying the HQE parameters. Then, a toy MC simulation is created, where the moments are randomly shifted according to their theoretical errors. The correlation matrix is calculated with equation 5.2. Finally, the individual entries in the matrix are multiplied by the total scale factor, which is computed by multiplying them with $\xi(q^2_{cut})$ from equation 5.3. The q^2_{cut} values are separated by $0.5\,\mathrm{GeV}^2$ and the first q^2_{cut} value is the lower one of the two moments plus an offset of $0.25\,\mathrm{GeV}^2$. For q^2_{cut} values of $1.5\,\mathrm{GeV}^2$ and $7.5\,\mathrm{GeV}^2$, the total scale factor is calculated as $\prod_{k=0}^{k=11} \xi(1.75 + 0.5 \times k\,\mathrm{GeV}^2) \approx 0.61$.

5.3 Constraints

External constraints on the HQE parameters from other experiments reduce the overall error of the fit and mitigate ambiguity due to the theoretical correlations. The moments of semileptonic decays are primarily sensitive to a linear combination of the heavy quark masses m_b and m_c. The dependency of the moments can be approximated as $\approx m_b - 0.8 m_c$. Therefore, it is essential to constrain at least one of the masses, as otherwise, they could take on arbitrary values and compensate for each other.

Constraints for fit on only q^2 moments

In this thesis, both heavy quark masses are constrained by the Flavour Lattice Averaging Group (FLAG) review [79], since they are used for the computation of the moments. The FLAG $N_f = 2 + 1 + 1$ heavy quark masses are

$$\overline{m}_b^{(4)}(\overline{m}_b) = 4.203(11)\,\mathrm{GeV}, \qquad \overline{m}_c^{(4)}(3\,\mathrm{GeV}) = 0.989(10)\,\mathrm{GeV}. \tag{5.4}$$

Here, the number of active quark flavors n is indicated with the superscript (n), as it influences the conversion from the $\overline{MS}$ scheme to the kinetic scheme. The average value of the m_b mass is then converted to the kinetic scheme with option **B** in reference [80] and the three-loop correction of reference [81] to

$$m_b(1\,\mathrm{GeV}) = 4.562(18)\,\mathrm{GeV}. \tag{5.5}$$

The value $\overline{m}_c$ at 2 GeV has to be computed from the one at 3 GeV and results in

$$\overline{m}_c(2\,\mathrm{GeV}) = 1.094(11)\,\mathrm{GeV}. \tag{5.6}$$

This calculation is carried out using the `RunDec` package from reference [82], with the value for $\alpha_s^{(5)}(M_Z = 91.1880(20)) = 0.1180(9)$ from reference [5]. The value of $\alpha_s^{(4)}$ is also computed with `RunDec` at a dynamic energy scale of $\mu_{\alpha_s} = m_b^{kin}/2$, which is suggested by reference [7], since the physical scale of the decay is lower than m_b.

The chromomagnetic expectation value μ_G^2 is constrained by the B hyperfine splitting and the heavy quark sum loosely constrains ρ_{LS}^3. Following the suggestions and calculations in references [83] and [84], the constraints used in the fit are

$$\mu_G^2 = 0.35(7)\,\text{GeV}^2, \qquad \rho_{LS}^3 = -0.15(10)\,\text{GeV}^3. \tag{5.7}$$

For the determination of $|V_{cb}|$, the averaged mean lifetime of neutral and charged B mesons is used from reference [5]:

$$\tau_B = 1.578(4)\,\text{ps} \tag{5.8}$$

Constrains for validation fits

The reference fits use older values for the physical parameters. The individual constraints can be found in references [7], for the fit on E_l & m_X^2 moments, and [10], for the fit on E_l, m_X^2 & q^2 moments.

5.4 Fit Setup and χ^2 Function

The goal of the fit on moments from semileptonic inclusive decays is to determine the HQE parameters and $|V_{cb}|$. The computations of the moments and semileptonic width in Section 5.1 take the HQE parameters as input. These computed moments can then be compared with the experimentally measured moments. By varying the input data of the theory model computations, the fit tries to minimize the discrepancy between the measured data and the model's predictions.

This thesis uses the minimization tool `iMinuit` [85], which is based on algorithms from reference [86], to minimize a χ^2 function. The full χ^2 function accounts for the moments measured by the experiments, the experimental and theoretical errors, as well as their correlations and the constraints on the HQE parameters. The parameters being fitted include m_b^{kin}, $\overline{m}_c(2\,\text{GeV})$, μ_π^2, ρ_D^3, μ_G^2, ρ_{LS}^3, $BR_{cl\nu}$ and $|V_{cb}|$. The function takes the form

$$\begin{aligned}\chi^2(\boldsymbol{\theta}) =& (\boldsymbol{M}(\boldsymbol{\theta}) - \boldsymbol{M}_{meas}) C^{-1} (\boldsymbol{M}(\boldsymbol{\theta}) - \boldsymbol{M}_{meas})^T \\ &+ \sum_{i=1}^{4} \frac{(\theta_i - \theta_i^{cons})^2}{\sigma_{\theta_i}^2} + \frac{(0.01 BR_{cl\nu}/\Gamma_{sl} - \tau_B)^2}{\sigma_{\tau_B^\star}^2},\end{aligned} \tag{5.9}$$

m_b^{kin}	$\overline{m}_C(2\,\mathrm{GeV})$	μ_π^2	ρ_D^3	μ_G^2	ρ_{LS}^3	$BR_{cl\nu}$	$\lvert V_{cb}\rvert$
4.6	1.0	0.4	0.2	0.35	-0.15	10.78	0.0417

Table 5.4: Initial parameters for all fits in this thesis.

where $\boldsymbol{\theta}$ are the HQE parameters to be fitted, $\boldsymbol{M}(\boldsymbol{\theta})$ are the computed moments, $\boldsymbol{M}_{meas}$ are the measured moments, $C = C_{theo} + C_{exp}$ is the covariance matrix constructed from both theoretical and experimental errors and their correlations, and $\theta_i^{cons} = m_b^{kin}, \overline{m}_c, \mu_G^2, \rho_{LS}^3$ and $\sigma_{\theta_i}^2$ are the constraints from section 5.3. The last term in equation 5.9 is the constrained lifetime of the B mesons, with the computed semileptonic width Γ_{sl} and the modified error $\sigma_{\tau_B^*}$. The error for τ_B is adjusted to account for the error in the computation of Γ_{sl} and is calculated by the square root of the squared sum from the individual errors stemming from τ_B and Γ_{sl} [7].

The fit procedure begins by computing the theoretical errors and correlation with the initial parameters, shown in Table 5.4. Next, the fit routine is run using `iMinuit`, which computes the HQE parameters that minimize the χ^2 function of equation 5.9. Afterward, the theoretical errors and correlations are recalculated using the newly fitted parameters. The fit routine is then rerun with the updated covariance matrix. This iteration continues until the change in the function value of χ^2 is minimal, ensuring that the correlation and errors are evaluated near the functional minimum. In this thesis, the threshold for exiting the loop is set to $|\Delta\chi^2| < 10^{-3}$.

5.4.1 Corrections

Since the publication of the code for the leptonic and hadronic moments, as well as the measured moments, corrections have been computed to account for additional effects.

First, the computation of the E_l and m_X^2 moments from reference [77, 6] missed contributions from two-loop charm effects. These effects were computed in reference [80] and can be included by shifting the values of m_b^{kin}, μ_π^2 and ρ_D^3. The shifts are calculated using the following formulas:

$$\Delta m_b^{kin} = \frac{2}{27 m_b^{kin}} \left(\frac{\alpha_s}{\pi}\right)^2 \mu_{kin}(8 m_b^{kin} + 3\mu_{kin}) \log \frac{\mu_{\alpha_s}}{m_c^{pole}}, \tag{5.10}$$

for the shift in m_b;

$$\Delta \mu_\pi^2 = -\frac{4}{3} \left(\frac{\mu_{kin}\alpha_s}{\pi}\right)^2 \log \frac{\mu_{\alpha_s}}{m_c^{pole}}, \tag{5.11}$$

for the shift in μ_π^2;

$$\Delta\rho_D^3 = -\frac{8}{27}\frac{\mu_{kin}^3\alpha_s^2}{\pi^2}\log\frac{\mu_{\alpha_s}}{m_c^{pole}}, \tag{5.12}$$

for ρ_D^3. Here, $m_c^{pole} = 1.3\,\text{GeV}$ is the pole mass of the charm quark. In the fit procedure, the shifts to the three parameters are applied after the computation of the E_l & m_X^2 moments, but before the computation of the q^2 moments and Γ_{sl}.

Next, QED corrections to the leptonic moments have been computed in reference [87]. A small difference was found between BaBar's estimations of the inclusive branching fraction based on `Photos`[88] and the more precise calculation. The updated branching fraction for BaBar measurements is given by:

$$R_{QCD}^{new} = \zeta_{QED}R_{QED}^{BaBar}. \tag{5.13}$$

In reference [10], the corrections for different values of E_{cut} were computed, resulting in the following values:

$$\zeta_{QED}(0.6\,\text{GeV}) = 0.9918, \quad \zeta_{QED}(1.2\,\text{GeV}) = 0.9969, \quad \zeta_{QED}(1.5\,\text{GeV}) = 1.0010. \tag{5.14}$$

These corrections are applied to the R^* values of the BaBar measurements for the fit on E_l, m_X^2 & q^2 moments in this thesis. The corrections for the leptonic moments of BaBar influence the fit only minimally and are therefore ignored [10]. Belle employs similar methods as BaBar to subtract QED effects, but the sizes of their contributions are not available, so no corrections have been computed for their data.

Finally, corrections arising from the $\mathcal{O}(\alpha_s^3)$ contribution, computed in reference [89], have been considered. An investigation of the theoretical uncertainties of the moments showed that the $\mathcal{O}(\alpha_s^3)$ contributions are well within the estimated error for most moments. The only exception is for the third hadronic moment, where the uncertainties are sometimes smaller than the computed $\mathcal{O}(\alpha_s^3)$ contributions, which are larger than 25%. In these cases, the error for the third hadronic moment is set to 30% if it falls below this threshold. These uncertainties are updated whenever the theoretical errors and correlations are recalculated.

Chapter 6

Validation Fits Results

To validate the fitting procedure, a fit on E_l & m_X^2 moments and a fit on E_l, m_X^2 & q^2 moments are performed. In this chapter, the two results are presented and compared to the available fits in references [7] and [10]. The fits yield values for the HQE parameters μ_π^2, μ_G^2, ρ_D^3, and ρ_{LS}^3, along with the bottom quark mass in the kinetic scheme, $m_b^{kin}(1\,\text{GeV})$, and the charm quark mass in the $\overline{MS}$ scheme, $\overline{m}_c(2\,\text{GeV})$. Additionally, the inclusive semileptonic branching ratio, $BR_{cl\nu}$, and the CKM matrix element, $|V_{cb}|$, are determined. Section 6.1 presents the fit results using E_l & m_X^2 moments. The results that incorporate q^2 moments into the fit are shown in Section 6.2. Additional results for the validation fits are shown in Section 6.3.

6.1 E_l & m_X^2 Validation Fit

The applied constraints and physical parameters for this fit are summarized in Table 6.1. They are chosen to match the constraints and corrections used in reference [7].

This section presents the results of the fit performed on E_l & m_X^2 moments, using

μ_{kin}	1 GeV	μ_c	2 GeV
μ_{α_s}	$m_b^{kin}/2$	τ_B	1.579(5) ps
$\alpha_s^{(5)}(m_Z)$	0.1179(10)	m_Z	91.188(2) GeV
m_b^{kin}	4.565(19) GeV	$\overline{m}_c(2\,\text{GeV})$	1.093(8) GeV
μ_G^2	0.35(7) GeV^2	ρ_{LS}^3	$-0.15(10)$ GeV^3
$\Delta m_b^{kin}/\mu_\pi^2/\rho_D^3$	✓	R^*_{BaBar}	✗
h_3	✗		

Table 6.1: Constraints and corrections defined for the E_l & m_X^2 fit of this thesis. Checkmarks indicate that the correction was applied and crosses show the not used ones. The values and corrections match the ones from reference [7].

m_b^{kin}	$\overline{m}_c(2\text{GeV})$	μ_π^2	ρ_D^3	μ_G^2	ρ_{LS}^3	$BR_{cl\nu}$	$10^3\lvert V_{cb}\rvert$
4.574	1.092	0.474	0.185	0.303	-0.13	10.66	42.13
0.012	0.008	0.056	0.030	0.049	0.092	0.15	0.51
1.0	0.295	-0.15	0.042	0.624	-0.197	-0.067	-0.425
	1.0	0.022	-0.006	-0.152	0.046	0.027	0.059
		1.0	0.735	-0.062	0.069	0.174	0.432
			1.0	-0.161	-0.148	0.092	0.301
				1.0	0.002	0.011	-0.229
					1.0	-0.033	-0.005
						1.0	0.682
							1.0

Table 6.2: Fit results for E_l & m_X^2 moments with the symmetric correlation matrix.

all 50 measurements summarized in Table 4.1. Table 6.2 summarizes the results of the standard fit to E_l & m_X^2 moments, including the estimated values of fit parameters and their standard errors in the first two rows. The lower portion presents the symmetric correlation matrix, which quantifies the dependencies between the parameters. The chi-square value for this fit is $\chi^2 = 22.285$, yielding a reduced chi-square of $\chi^2/d.o.f. = 0.531$, indicating a good fit. The degrees of freedom $(d.o.f)$ are defined as $d.o.f = N_{meas} - N_{para}$, where N_{meas} is the number of measurements and N_{para} is the number of fitted parameters.

The correlation matrix shows strong dependencies among certain parameters. Notably, m_b^{kin} and μ_G^2 have a correlation coefficient of 0.624, while μ_π^2 and ρ_D^3 are more strongly correlated, with a coefficient of 0.735. A significant correlation is also observed between $BR_{cl\nu}$ and $|V_{cb}|$, with a coefficient of 0.682. This strong correlation is expected, as $BR_{cl\nu}$ is used for the constraint on $|V_{cb}|$ by τ_B.

The inclusion of the two-loop charm effects from [80] leads to minor shifts in the fit parameters: m_b^{kin} increases by $+0.003\,\text{GeV}$, while μ_π^2 and ρ_D^3 decrease by $-0.002\,\text{GeV}^2$ and $-0.001\,\text{GeV}^3$, respectively. Table 6.2 presents the fit results after applying these shifts. In the computation the shifts are applied after the E_l & m_X^2 moments have been computed and before the calculation of Γ_{sl}.

Comparing this result to `TABLE I` in reference [7] shows very strong similarities. The central values of the HQE parameters μ_π^2, μ_G^2, as well as m_b^{kin} and $|V_{cb}|$ differ only in the last decimal point, which translates to a difference below 1%. The uncertainties match almost perfectly and the correlation matrix is also very similar.

The conclusion is that the fit on E_l & m_X^2 moments of this thesis works, as it can reproduce the same values as in reference [7].

μ_{kin}	1 GeV	μ_c	2 GeV
μ_{α_s}	$m_b^{kin}/2$	τ_B	1.579(5) ps
$\alpha_s^{(5)}(m_Z)$	0.1179(9)	m_Z	91.188(2) GeV
m_b^{kin}	4.562(18) GeV	$\overline{m}_c(2\,\text{GeV})$	1.094(11) GeV
μ_G^2	0.35(7) GeV^2	ρ_{LS}^3	$-0.15(10)$ GeV^3
$\Delta m_b^{kin}/\mu_\pi^2/\rho_D^3$	✓	R^*_{BaBar}	✓
h_3	✓		

Table 6.3: Constraints and corrections defined for the E_l, m_X^2 & q^2 fit of this thesis. Checkmarks indicate that the correction was applied and crosses show the not used ones. The values and corrections match the ones from reference [10].

m_b^{kin}	$\overline{m}_c$(2GeV)	μ_π^2	ρ_D^3	μ_G^2	ρ_{LS}^3	$BR_{cl\nu}$	$10^3\lvert V_{cb}\rvert$
4.574	1.090	0.457	0.181	0.285	-0.122	10.61	41.91
0.012	0.010	0.043	0.020	0.049	0.090	0.15	0.49
1.0	0.373	-0.225	-0.017	0.560	-0.171	-0.063	-0.426
	1.0	0.013	-0.047	-0.229	0.079	0.031	0.075
		1.0	0.537	-0.093	0.232	0.139	0.34
			1.0	-0.257	-0.027	0.024	0.146
				1.0	0.010	0.004	-0.253
					1.0	-0.012	0.055
						1.0	0.686
							1.0

Table 6.4: Fit results of E_l, m_X & q^2 moments with the symmetric correlation matrix.

6.2 E_l, m_X^2 & q^2 Validation Fit

The applied constraints and physical parameters for this fit are summarized in Table 6.3. They are chosen to match the constraints used in reference [10]. Additionally, it is important to note that the fit of this thesis only utilizes the Belle data of the electron channel and does not include the muon channel. Reference [10] used an averaged set of both channels from Belle. These averaged moments are not available to the public as of the writing of this thesis. For validation of the fit procedure, the electron channel was selected, as most semileptonic decays of B meson produce an electron. The Belle II q^2 moments include already all measured leptons.

The results of the fit on E_l, m_X & q^2 moments are shown in table 6.4. The χ^2 value is 36.328, which corresponds to a $\chi^2/d.o.f$ of 0.527. The correlation matrix indicates strong correlations between m_b^{kin} and μ_G^2 (0.560) and $BR_{cl\nu}$ and $|V_{cb}|$ (0.686), around the same magnitude as the fit on only E_l & m_X^2 moments.

Comparing this result to **Table 4** in reference [10] shows strong similarities, but

small deviations are more visible. The uncertainties match almost perfectly and the correlation matrix is also very similar. The central values of the fit parameters differ only in the last decimal point, which translates to a difference below 1%. Only for ρ^3_{LS} is increased by about 8% compared to the fit of reference [10]. Compared to the relative error $\Delta\rho^3_{LS}/\rho^3_{LS} = 74\%$, this shift of 8% is well within the error limit.

The fit in this thesis uses only the electron channel, rather than an averaged set of the electron and muon channels. Since the results remain compatible with other published results, this suggests that the influence of muons on the fit outcome is minor.

The conclusion is that the fit of this thesis on E_l, m^2_X & q^2 moments works, as it can reproduce the same values as in reference [10]. This assumption is further supported by comparing the results of the fit that only uses the Belle II q^2 data. Reference [10] provides results for fits on only Belle II data with constraints from previous fits, which are summarized in Table 6.1. The results from this thesis are in good agreement with the results of reference [10].

	m_b^{kin}	$\overline{m}_c$(2GeV)	μ^2_π	ρ^3_D	μ^2_G	ρ^3_{LS}	$BR_{cl\nu}$	$10^3\|V_{cb}\|$
Belle II	4.573	1.092	0.462	0.177	0.301	-0.122	10.65	42.07
this thesis	0.012	0.008	0.044	0.02	0.049	0.09	0.15	0.49
Belle II	4.573	1.092	0.460	0.175	0.303	-0.118	10.65	42.08
Finauri et al. [10]	0.012	0.008	0.044	0.020	0.049	0.090	0.15	0.48

Table 6.5: Results for a fit including E_l, m^2_X and q^2 moments from only Belle II, compared to the results of reference [10].

6.3 Additional Results for Validation Fits

Analysis for Correction to Measurements and Theory

Additionally, the impact of updated theoretical error corrections for the third hadronic moments on the E_l & m^2_X fit was investigated. Table 6.6 presents the fit results when theoretical corrections on third hadronic moments are included. The constraints used for this fit correspond to Table 6.3. Although parameter uncertainties slightly increase with these corrections, notable shifts are observed: ρ^3_D increases by nearly 13% and ρ^3_{LS} decreases by 11%. While the change in ρ^3_{LS} can be neglected due to the large error of this parameter, the change in ρ^3_D is around the same magnitude as its relative error.

The consistency of $|V_{cb}|$ values, both with and without theoretical corrections, suggests that the impact of these corrections on the extraction of $|V_{cb}|$ is minimal within the reported uncertainties.

m_b^{kin}	$\overline{m}_c$(2GeV)	μ_π^2	ρ_D^3	μ_G^2	ρ_{LS}^3	$BR_{cl\nu}$	$10^3\|V_{cb}\|$
4.576	1.090	0.494	0.209	0.286	-0.144	10.63	42.06
0.013	0.010	0.060	0.036	0.051	0.094	0.15	0.52

Table 6.6: Fit results for E_l & m_X^2 moments with corrections to the measurements applied. The full list of constraints is shown in Table 6.3.

Analysis of Error Iteration

An examination of the first iteration of the fit on all moments reveals slight differences compared to the final results obtained after updating the theoretical values. In this initial iteration, the fit on E_l, m_X^2 & q^2 moments yields $\chi^2/d.o.f = 0.507$, with the parameter values shown in Table 6.7. This result suggests that the fit is already near the minimum after the first iteration and indicates a good convergence.

m_b^{kin}	$\overline{m}_c$(2GeV)	μ_π^2	ρ_D^3	μ_G^2	ρ_{LS}^3	$\text{BR}_{cl\nu}$	$10^3\|V_{cb}\|$
4.574	1.090	0.463	0.185	0.285	-0.128	10.61	41.93
0.007	0.010	0.046	0.023	0.047	0.090	0.15	0.47

Table 6.7: Fit results of E_l, m_X & q^2 moment with the initial conditions as a basis for the calculation of theory errors and correlations.

Chapter 7

Results for q^2 Fits

This chapter presents the fit results for inclusive semileptonic decay observables using only q^2 moments. The fits yield values for the HQE parameters μ_π^2, μ_G^2, ρ_D^3, and ρ_{LS}^3, along with the bottom quark mass in the kinetic scheme, $m_b^{kin}(1\,\text{GeV})$, and the charm quark mass in the $\overline{MS}$ scheme, $\overline{m}_c(2\,\text{GeV})$. Additionally, the inclusive semileptonic branching ratio, $BR_{cl\nu}$, and the CKM matrix element, $|V_{cb}|$, are determined. Section 7.1 reports the results from fits using only q^2 moments, based on Belle and Belle II data. Finally, Section 7.2 compares the q^2 fit with the validation fits and examines the contributions of experimental and theoretical uncertainties.

7.1 Fit Results for q^2 Moments

With the fit procedure validated by the two fit results in Tables 6.2 and 6.4, the fit procedure can now be used with only q^2 moments. The standard constraints used for the fit on only q^2 moments are summarized in Table 7.1.

μ_{kin}	1 GeV	μ_c	2 GeV
μ_{α_s}	$m_b^{kin}/2$	τ_B	1.578(4) ps
$\alpha_s^{(5)}(m_Z)$	0.1180(9)	m_Z	91.188(2) GeV
m_b^{kin}	4.562(18) GeV	$\overline{m}_c(2\,\text{GeV})$	1.094(11) GeV
μ_G^2	0.35(7) GeV^2	ρ_{LS}^3	$-0.15(10)$ GeV^3

Table 7.1: Constraints and corrections defined for the q^2 fit of this thesis. The corrections from the previous fits only apply to the computations and measurements of E_l & m_X^2 moments.

The results of the fit are shown in Table 7.2. The chi-squared function has a value of $\chi^2 = 14.123$ and $\chi^2/d.o.f = 0.743$. The fit results of $\mu_\pi^2 = (-0.212 \pm 6.392)\,\text{GeV}^2$ deviates significantly from the other results. Although the mean values of $\text{BR}_{cl\nu}$

and $|V_{cb}|$ are in good agreement with the other results, their uncertainties are six to ten times larger than the results for only lepton and hadron moments, with $BR_{cl\nu} = 10.68 \pm 1.55$ and $|V_{cb}| = (41.95 \pm 3.06) \times 10^{-3}$.

This can be explained by the insensitivity of the q^2 moments to μ_π^2 and the fit with the standard settings results in large uncertainties for μ_π^2, $\mathrm{BR}_{cl\nu}$ and $|V_{cb}|$.

m_b^{kin}	$\overline{m}_c(2\mathrm{GeV})$	μ_π^2	ρ_D^3	μ_G^2	ρ_{LS}^3	$BR_{cl\nu}$	$10^3\|V_{cb}\|$
4.566	1.092	-0.217	0.148	0.330	-0.141	10.67	41.95
0.016	0.011	6.313	0.026	0.062	0.099	1.53	3.02
1.0	0.138	0.035	0.252	0.241	-0.066	0.038	-0.038
	1.0	-0.010	-0.172	-0.138	0.038	-0.010	0.010
		1.0	0.011	0.001	-0.001	-0.495	0.497
			1.0	-0.403	0.110	0.011	-0.011
				1.0	0.07	0.002	-0.002
					1.0	-0.001	0.001
						1.0	0.496
							1.0

Table 7.2: Fit results of q^2 moments with the constraints in Table 7.1.

References [9, 10] applied constraints on μ_π^2 and included measurements of the branching fraction $BR_{cl\nu}$, to contain the error. The approach of this thesis differs by using the fitted values of the fit on all moments from Table 6.4. This leads to the constraints of $\mu_\pi^2 = 0.457(43)\,\mathrm{GeV}^2$ and $BR_{cl\nu} = 10.61(15)$. These constraints stabilize the fit and reduce large uncertainties associated with unconstrained parameters.

The results for the fit to only q^2 moments, with μ_π^2 and $BR_{cl\nu}$ constrained, are summarized in Table 7.3. The χ^2 value is 14.121, which corresponds to a $\chi^2/d.o.f$ of 0.743. The correlation values for μ_π^2 and $BR_{cl\nu}$ are 0, when they are constrained. This indicates that these parameters are treated as independent from the other variables within the fit.

The values of $|V_{cb}|$ are

$$\begin{aligned} |V_{cb}| &= (42.15 \pm 0.54) \times 10^{-3} \qquad \text{with constraints,} \\ |V_{cb}| &= (41.95 \pm 3.02) \times 10^{-3} \qquad \text{without constraints.} \end{aligned} \tag{7.1}$$

The stability of the HQE parameters across fits suggests that the applied constraints primarily reduce uncertainties without introducing significant biases in the parameter estimates, but that their correlations change. For the fit with the additional constraints in Table 7.3, m_b^{kin} is highly negatively correlated to $|V_{cb}|$ (-0.606).

The fit with standard setting in Table 7.2 shows almost no correlation between m_b^{kin}-$|V_{cb}|$ (-0.038). The correlation of μ_π^2-$|V_{cb}|$ vanishes for μ_π^2 constrained and the correlation of $BR_{cl\nu}$-$|V_{cb}|$ remains in the same order of magnitude for the constrained and unconstrained fit.

m_b^{kin}	$\overline{m}_c$(2GeV)	μ_π^2	ρ_D^3	μ_G^2	ρ_{LS}^3	$BR_{cl\nu}$	$10^3\|V_{cb}\|$
4.566	1.092	0.457	0.148	0.330	-0.142	10.61	42.15
0.015	0.011	0.043	0.026	0.062	0.099	0.15	0.54
1.0	0.126	0.0	0.234	0.222	-0.061	0.0	-0.581
	1.0	0.0	-0.179	-0.145	0.039	0.0	0.183
		1.0	0.0	0.0	0.0	0.0	0.039
			1.0	-0.418	0.113	0.0	-0.165
				1.0	0.072	0.0	-0.007
					1.0	0.0	0.013
						1.0	0.552
							1.0

Table 7.3: Fit results of q^2 moments with the symmetric correlation matrix. μ_π^2 and $BR_{cl\nu}$ were constrained by the values from the fit of all moments in Table 6.4.

The HQE parameters of the only q^2 fits match, within their uncertainties, with the parameters extracted from the other fits (see Tables 6.2 and 6.4), except ρ_D^3. The difference between the two central values is around 1σ. Compared to the below 1σ differences for the other parameters, there seems to be an ambiguity.

7.1.1 Including Muon Data from Belle

For the validation on all moments, the inclusion of the μ data from Belle was not required, as the fit with only electron data from Belle already showed that the fitting procedure works. As no fit on only q^2 moments is published with this framework (reference [9] uses the RPI method) the effects of the μ data should be investigated. Repeating the fit with the standard settings in Table 7.1 and swapping the electron data with the muon data results in a fit with $\chi^2 = 16.679$ and $\chi^2/d.o.f = 0.878$. The fitted parameters, for standard settings and $\mu_\pi^2/BR_{cl\nu}$ constraints included, are shown in Table 7.4.

Compared to the fit with no muon data in Tables 7.3 and 7.2 the values of the HQE parameters do not change much. This indicates that the fit is stable regardless of the choice of lepton.

	m_b^{kin}	$\overline{m}_c$(2GeV)	μ_π^2	ρ_D^3	μ_G^2	ρ_{LS}^3	$BR_{cl\nu}$	$10^3\|V_{cb}\|$
standard settings	4.570	1.091	-0.110	0.157	0.314	-0.135	10.70	41.91
	0.016	0.011	6.298	0.027	0.063	0.099	1.53	3.01
standard setting and	4.570	1.091	0.457	0.157	0.314	-0.135	10.61	42.01
μ_π^2, $BR_{cl\nu}$ constraints	0.016	0.011	0.043	0.027	0.063	0.099	0.15	0.56

Table 7.4: Fit results of q^2 moments with muon instead of electron data from Belle. The first two rows show the central value and uncertainties of the fitted parameters from a fit with the standard settings from Table 7.1. For the fitted values from the last two rows, the constraints $\mu_\pi^2 = 0.457(43)\,\text{GeV}$ and $BR_{cl\nu} = 10.61(15)$ were applied additionally to the fit.

7.2 Confidence Region and Error Investigation

The construction of a standard error ellipse relies on the covariance matrix of the parameter estimates. The shape and orientation of the ellipse depend on the variances of the individual parameters and the covariance between them. The axes of the ellipse represent the directions of the greatest uncertainty, and they are centered about the corresponding mean center value from the fits.

A standard error ellipse is constructed by drawing an ellipse around the parameter estimates at a certain confidence region. The contour corresponds to $\chi^2 = \chi^2_{min} + 1$ and comprises a probability of 68.27% [5]. This means that if the experiment was repeated many times, the true parameter values would fall within the ellipse in 68.27% of the cases. The orientation of the ellipse also indicates the correlation between the parameters: if the parameters are highly correlated, the ellipse will be elongated, whereas if they are uncorrelated, the ellipse will be more circular.

In Figures 7.1 and 7.2, these confidence regions are used to visualize the relationships between specific pairs of parameters. In the plots in Figure 7.1 the relationships of m_b^{kin} with the other fit parameters are shown. The blue region corresponds to the fit on only q^2 moments and is larger for all parameters, compared to the fits on E_l & m_X^2 (orange and green), and E_l, m_X^2 & q^2 moments. This observation fits with the larger uncertainties of the parameters for the q^2 fit.

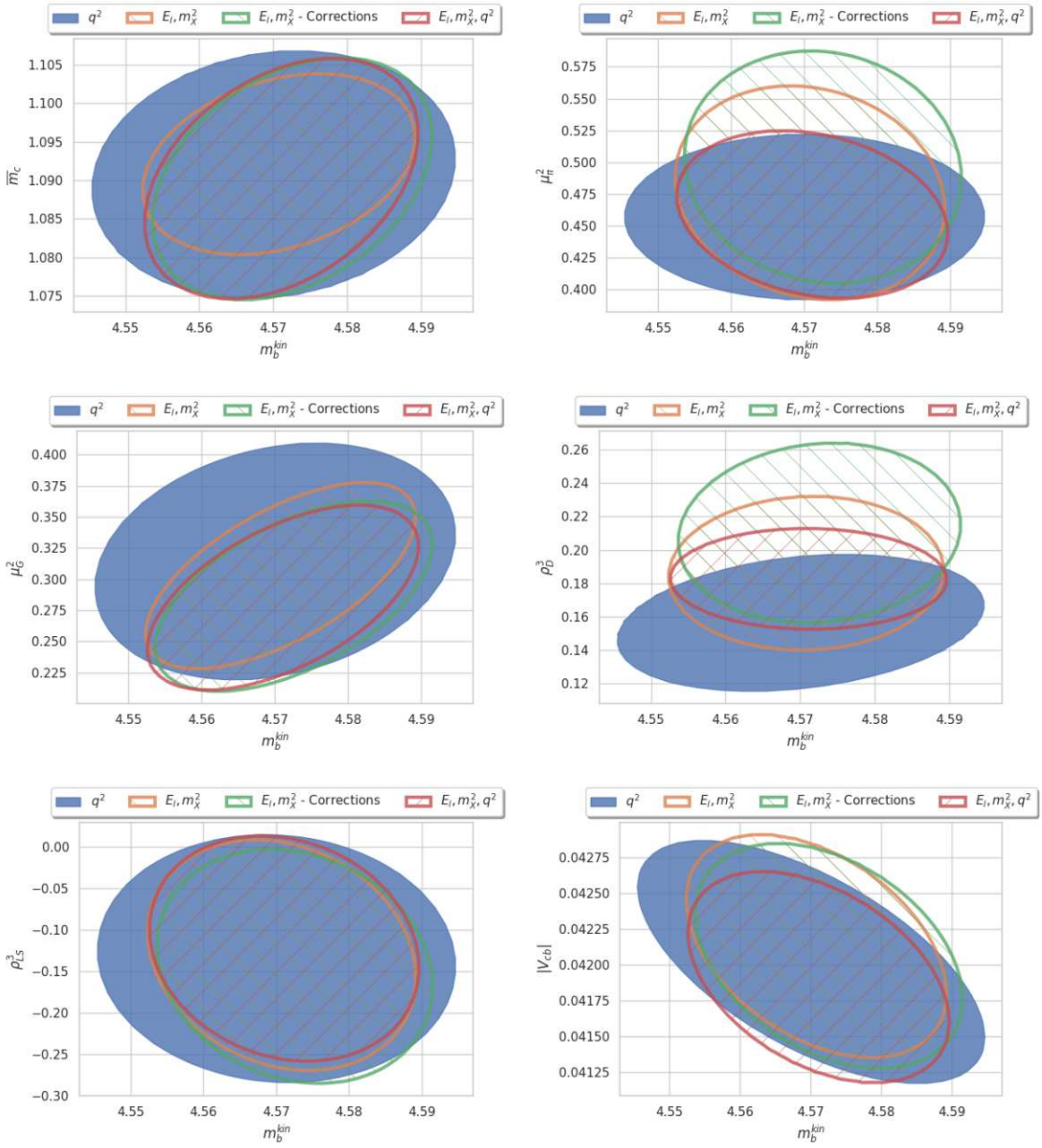

Figure 7.1: Regions of $\Delta\chi^2 < 1$ in the 2D planes (m_b^{kin}, m_c) (upper left), (m_b^{kin}, μ_π^2) (upper right), (m_b^{kin}, μ_G^2) (middle left), (m_b^{kin}, ρ_D^3) (middle right), (m_b^{kin}, ρ_{LS}^3) (lower left) and $(m_b^{kin}, |V_{cb}|)$ (lower right). The blue region corresponds to the fit on only q^2 with additional constraints on $BR_{cl\nu}$ and μ_π^2. E_l & m_X fits are shown in orange (without correction) and green (with the corrections). The red outline corresponds to the fit on E_l, m_X & q^2 moments.

The only parameter to not fit exactly with the other fits is ρ_D^3. The plots in Figure 7.2 show that the fit on q^2 moments prefers another direction in the parameter space for ρ_D^3. The discrepancy is especially visible when compared to the fit on E_l & m_X^2 moments with corrections (green). The corrections correspond to the QED calculations of the branching fraction R^* and updated theoretical uncertainties of h_3, presented in Section 5.4.1.

Notably, the uncertainty in ρ_D^3 for all fits is smaller than the 20% safety margin used in computing theoretical errors. The relative errors of ρ_D^3 from the fits on only q^2 moments and only E_l & m_X^2 are closest to the value of 20%, with $\Delta\rho_D^3/\rho_D^3 = 17.6\%$ and $\Delta\rho_D^3/\rho_D^3 = 16.2\%$. For the fit on all moments, the relative error is even lower at around 9%. All other HQE parameters have a relative error, which is higher than the safety shift introduced in section 5.2.

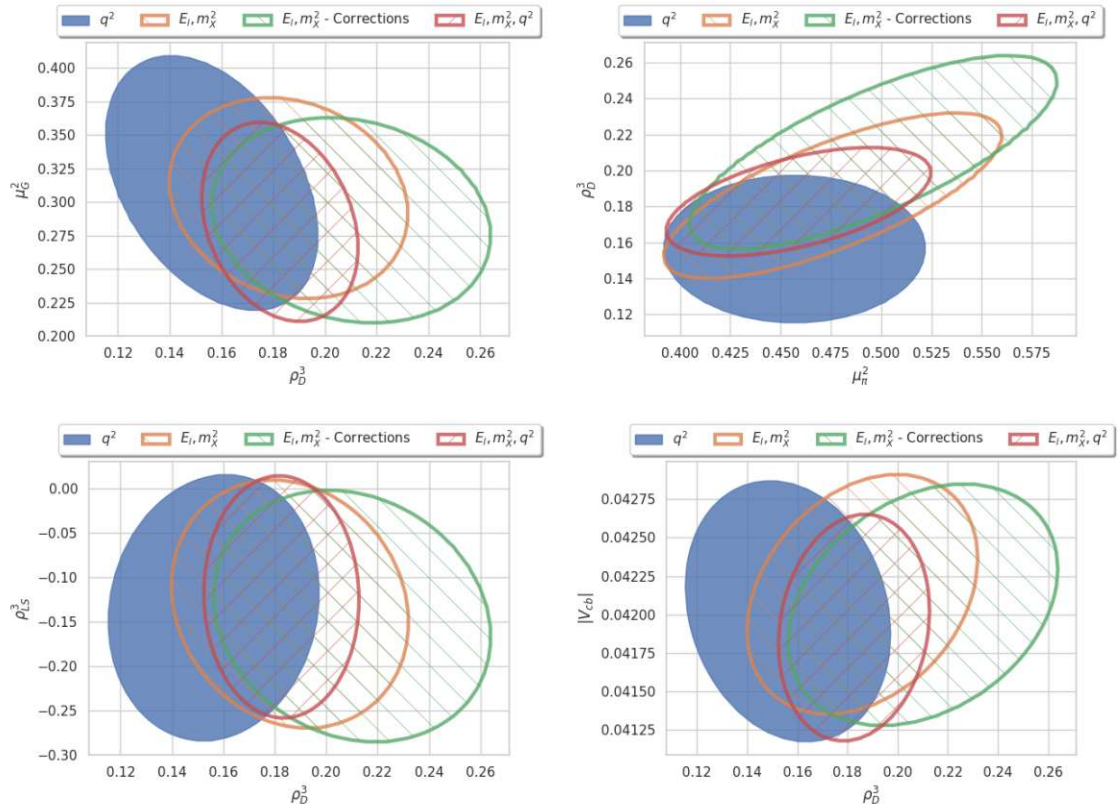

Figure 7.2: Regions of $\Delta\chi^2 < 1$ in the 2D planes (ρ_D^3, μ_G^2) (upper left), (μ_π^2, ρ_D^3) (upper right), (ρ_D^3, ρ_{LS}^3) (lower left) and (ρ_D^3 , $|V_{cb}|$) (lower right). The blue region corresponds to the fit on only q^2 with additional constraints on $BR_{cl\nu}$ and μ_π^2. E_l & m_X fits are shown in orange (without correction) and green (with the corrections). The red outline corresponds to the fit on E_l, m_X & q^2 moments.

The uncertainties in the parameters shown in tables 6.2, 7.3 and 6.4 come from experimental and theoretical errors. To better understand the sources of uncertainty, experimental and theoretical errors are analyzed separately. They can be differentiated by varying the experimental input data for the E_l, m_X^2 and q^2 moments within their experimental error. A multidimensional Gaussian distribution is generated using the experimental correlations and errors as inputs. The fit is performed using this randomly generated input data. Repeating this step results in a Gauss distribution for the HQE parameters. The total covariance matrix is set to the one from the original fit and is not updated during the iteration process. The results of $|V_{cb}|$ for the fit on only q^2 moments are illustrated in Figure 7.3. For this example, a total of 4500 input values were simulated. A Gaussian distribution is then fitted to this distribution and the standard deviation is then identified as the experimental error of the parameter.

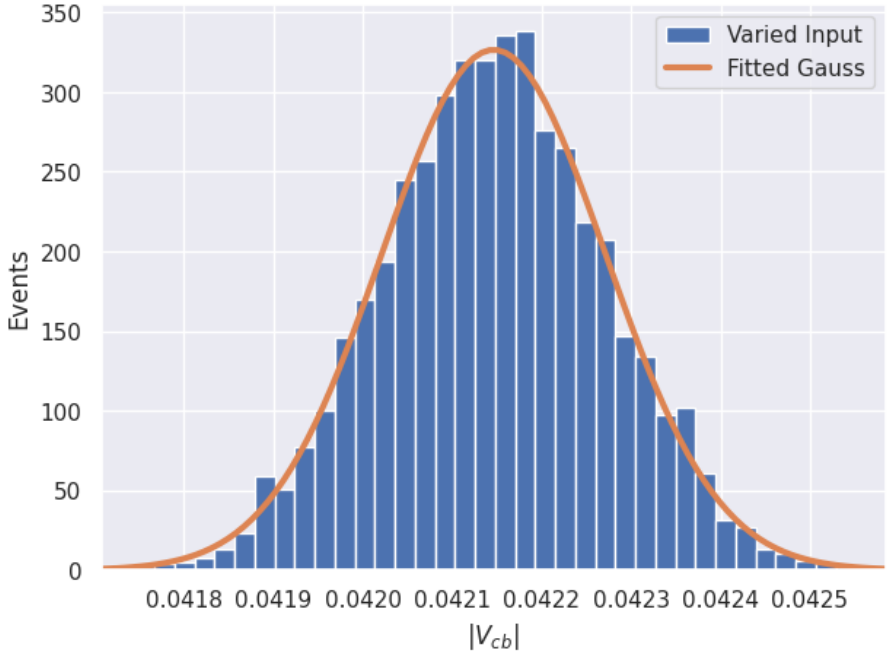

Figure 7.3: Distribution of $|V_{cb}|$ with the experimental varied q^2 input data performed fits and the fitted Gauss distribution. A total of 4500 different input parameters were simulated.

The theoretical uncertainties of $|V_{cb}|$ include among others the error stemming from the computation of the semileptonic width Γ_{sl}. The error of Γ_{sl} comes from higher-order contributions, that were not included in its calculation. In reference [7] the uncertainty in Γ_{sl} is estimated to be 1.2%. This error can then be expanded to an

uncertainty in $|V_{cb}|$. The formula for Γ_{sl} is proportional to $|V_{cb}|^2$, so the uncertainty of $|V_{cb}|$ stemming from Γ_{sl} is

$$\sigma_{|V_{cb}|}(\sigma_{\Gamma_{sl}}) = \left|\frac{d\Gamma_{sl}}{d|V_{cb}|}\right|^{-1} \sigma_{\Gamma_{sl}} = \frac{0.012|V_{cb}|}{2}. \tag{7.2}$$

The results for the experimental and Γ_{sl} error for all three different fits are shown in Table 7.5. The fit using only q^2 moments achieves a significantly smaller experimental error compared to the leptonic and hadronic moments fit, reflecting the more precise constraints provided by q^2 data. The q^2 data have a relative error of around 3.5% and the E_l & m_X^2 data of around 8%. The theoretical error includes all uncertainties that come from the theory error of the moments and the uncertainties in the HQE parameters. It is calculated by subtracting the squared uncertainties from the total fit error and taking the square root.

Moments	$\lvert V_{cb}\rvert \times 10^3$	Error	Experimental Error	Γ_{sl} Error	Theory Error
q^2	42.15	0.54	0.13	0.25	0.46
E_l, m_X	42.13	0.51	0.36	0.25	0.26
E_l, m_X,q^2	41.91	0.49	0.34	0.25	0.25

Table 7.5: Experimental, Γ_{sl} and theoretical error contributions to $|V_{cb}|$ from different fits. The theoretical error includes all error contributions that are not attributed to experimental and Γ_{sl} uncertainties.

Chapter 8

Conclusion and Outlook

This thesis extracts the HQE parameters and $|V_{cb}|$ from a fit on the leptonic invariant mass q^2 moments of inclusive semileptonic B decays of the form $B \to X_c l\nu$. To validate the fit procedure, a fit on the leptonic energy distribution E_l and hadronic invariant mass distribution m_X^2, and a fit including all three moments were carried out and compared to published results in references [7, 10]. Data for the E_l and m_X^2 moments were obtained from BaBar, Belle, CDF, CLEO, and DELPHI, while data for the q^2 moments were measured at Belle and Belle II. The theoretical computations of the moments are based on the OPE and are fitted to the experimental data. The OPE allows for the expression of products of operators at different spacetime points as a series of local operators. This expansion is performed in the heavy quark limit, yielding a series in $1/m_b$, with individual coefficients of the matrix elements further expanded in powers of α_s. The computations in this thesis include terms up to α_s^3 and $1/m_b^3$.

The experimental data are measured at different cut values of E_{cut}, for the lepton energy and hadronic mass distributions, and q^2_{cut}, for the leptonic invariant mass, allowing for more available measurements in the fit. This structure makes it necessary to consider the theoretical correlations between the moments. The correlation model used in this thesis follows option **D** from reference [78], where moments with different cut values are correlated by a factor ξ for each step between them, while moments of different types are treated as uncorrelated. The correlation factors are detailed in equations 5.1 for the E_l & m_X^2 moments and 5.3 for the q^2 moments.

Additional constraints were applied to stabilize the fit, particularly on μ_G^2 and ρ_{LS}^3. Due to the sensitivity of theoretical computations to a linear combination of m_b and m_c, at least one of these masses must be constrained. This thesis constrains both, using information from other measurements. The B meson mean lifetime τ_B was used in the extraction of $|V_{cb}|$.

The results for the validation fits are presented in Table 6.2 (for E_l & m_X^2 moments) and in Table 6.4 (for E_l, m_X^2 & q^2 moments). The fits match very well within

their uncertainty to the published results in references [7, 10] and validate the fitting procedure.

The results for the fit on only q^2 moments are presented in Table 7.2. This fit showed an insensitivity to the HQE parameter μ_π^2, which is reflected in the large uncertainty of this parameter and consequently $BR_{cl\nu}$ and $|V_{cb}|$. Constraints on μ_π^2 and $BR_{cl\nu}$, obtained from the fit on all moments, are able to stabilize the fit and the results for the fit on only q^2 moments with additional constraints are shown in Table 7.3. A comparison of HQE parameters across fits reveals varying sensitivities. A naive assumption that the combined fit is an average of the individual fits is disproven, as evidenced by the reduced sensitivity of q^2 moments to μ_π^2 and their preference for a lower value even in the combined fit. Other parameters, such as ρ_{LS}^3, show consistency across individual fits but increase by approximately 15% in the combined fit. Given its relative error of 74%, this shift is not significant, highlighting the minor role of ρ_{LS}^3 in the fit.

A notable challenge is the HQE parameter ρ_D^3, whose relative error ranges from 9% in the combined fit to about 17.6% in individual fits. The discrepancy in central values, particularly between the q^2 and $E_l\&m_X^2$ fits, is concerning. Figure 7.2 shows that the corresponding $\Delta\chi$ planes barely overlap, indicating distinct parameter space preferences. The combined fit's ρ_D^3 value lies near the average of the individual fits, suggesting similar sensitivities of q^2 and $E_l\&m_X^2$ moments to this parameter. Further investigation into higher-order terms or the inclusion of different moments could introduce new parameters that would solve this discrepancy between the values of ρ_D^3 from the q^2 and $E_l\&m_X^2$ fits.

All other parameters remain within the error bounds of each fit. The combined fit favors the m_b^{kin} value from the $E_l\&m_X^2$ fit, despite the constraint $m_b^{kin,\text{const}} = 4.562(18)\,\text{GeV}$.

The main results for $|V_{cb}|$ are:

$$\begin{aligned} |V_{cb}|_{q^2} &= 41.95(3.02) \times 10^{-3}, \\ |V_{cb}|_{q^2} &= 42.15(54) \times 10^{-3}\,(\mu_\pi^2 \text{ and } BR_{cl\nu} \text{ constrained}). \end{aligned} \tag{8.1}$$

This shows that an inclusive determination of $|V_{cb}|$ with a fit on only q^2 moments leads to results that are consistent with other inclusive determinations.

Another comparison can be made with the fit results on q^2 moments from reference [9], which employs a different methodology based on RPI. It is important to note that the use of RPI changes the definitions of the HQE Parameters and comparison requires including this change in basis. Additionally, they used measurements for the branching fraction $BR_{cl\nu}$. Furthermore, in their model, ρ_{LS}^3 gets absorbed by the RPI, which is why neither of these two parameters appears in their fit.

When comparing the results of reference [9] to Table 7.3 most parameters match,

m_b^{kin}	$\overline{m}_c(2GeV)$	μ_π^2	ρ_D^3	μ_G^2	$10^3\|V_{cb}\|$
4.56	1.09	0.43	0.03	0.38	41.70
0.02	0.01	0.24	0.02	0.07	0.65

Table 8.1: Results for fit on q^2 moments from reference [9].

except ρ_D^3. The central value of their fit is out of the error limits of all fits, even for the lower value from the q^2 fit. This clear difference shows that there is a discrepancy between the methods used in this thesis and the one from reference [9] that can not be explained by a change in basis. Generally, the q^2 moments seem to favor a lower value for ρ_D^3. This suggests that the OPE for the moments may not be as general as thought, or that still unknown parameters influence the determination.

An overall improvement in the extraction of the HQE parameters and $|V_{cb}|$ is anticipated with new measurements of the lepton energy distribution and hadronic invariant mass distribution. To date, these moments have not yet been measured by Belle II. An improved determination of the moments could reduce the error stemming from the experiment. The discrepancy in ρ_D^3 found in this thesis could be attributed to the difference in measurements since the q^2 moments were measured more accurately. Including additional observables, such as the charged lepton forward-backward asymmetry [90] or partial moment differences [91], could also resolve ambiguities and enhance $|V_{cb}|$ determination.

Higher-order contributions, like $\mathcal{O}(\alpha_s^3)$ terms for third hadronic moments [89], significantly affect calculations. Investigating even higher-order terms may improve series convergence. Additionally, q^2 moments contributions of $\mathcal{O}(\Lambda_{QCD}/m_b^4)$ and higher power could influence the extraction of $|V_{cb}|$. The investigation of these higher power terms for E_l and m_X^2 moments from reference [92] showed that these contributions have only a small effect on the fit. This suggests a limited influence on q^2 fits, but exact calculations have not been carried out yet.

The $|V_{cb}|$ values in equation 8.1 remain in tension with the results based on exclusive decays. Lattice QCD calculations for $B \to D^* l \overline{\nu}_l$ decays are consistent with each other and result in a lower value for $|V_{cb}|$, compared to inclusive decays [14, 93, 94, 13, 95]. The PDG reports an average of $|V_{cb}| = (39.8 \pm 0.6) \times 10^{-3}$ for exclusive B decays, with a 3σ difference, to equations and 8.1 [5]. Recent determinations of $|V_{cb}|$ from Belle and Belle II result in values closer to the inclusive decay fits, with a difference of 1σ [12, 11]. A comparison of the results of this thesis with selected published results for inclusive and exclusive determination is shown in Figure 8.1.

Despite extensive experimental and theoretical results for exclusive and inclusive decays, the V_{cb} puzzle still persists. New lattice QCD approaches to inclusive decays could provide fresh insights and resolve the discrepancy, which can be used to solve the V_{cb} puzzle [96, 97].

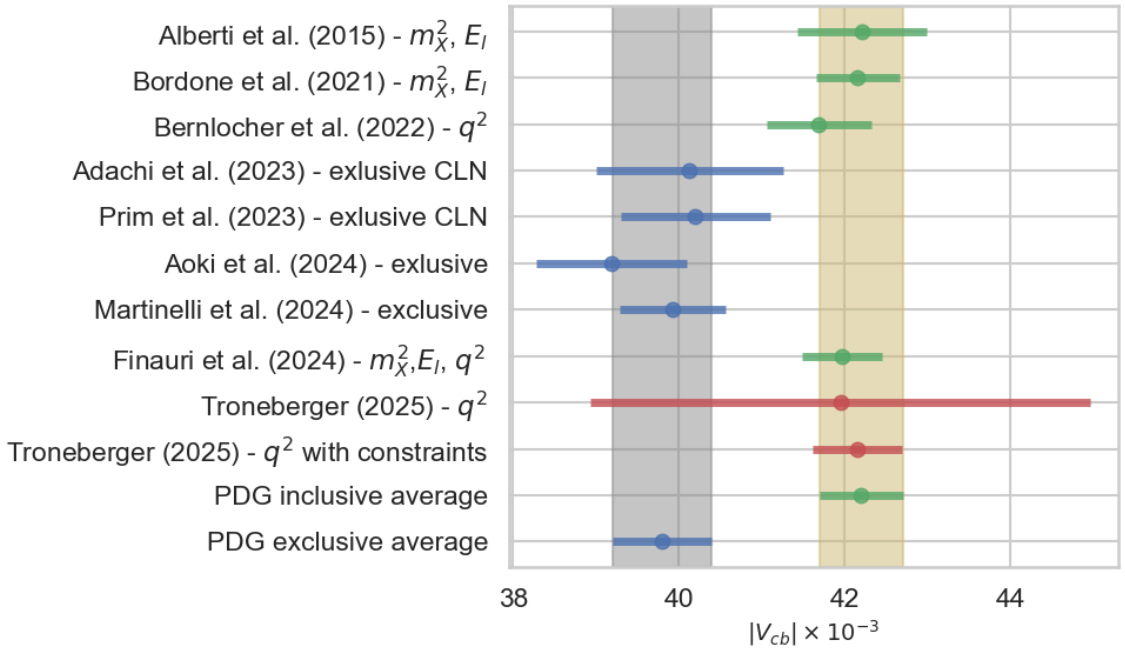

Figure 8.1: Recent values of $|V_{cb}|$ determined with exclusive (blue) and inclusive (green) methods. The values of Troneberger (red) are determined in this thesis. The shaded areas are exclusive (gray) and inclusive (beige) averages from the Particle Data Group (PDG) [5]. The references for the other values can be taken from Figure 1.2.

Bibliography

[1] Peter W. Higgs
"Broken symmetries and the masses of gauge bosons"
Physical Review Letters 13 (16 Oct. 1964), 1964, URL: https://journals.aps.org/prl/abstract/10.1103/PhysRevLett.13.508.

[2] G Aad et al.
"Observation of a new particle in the search for the Standard Model Higgs boson with the ATLAS detector at the LHC"
Physics Letters B 716 (1 2012), 2012, URL: https://doi.org/10.1016/j.physletb.2012.08.020.

[3] A.D. Sakharov
"Violation of CP Invariance, C asymmetry, and baryon asymmetry of the universe"
Pisma Zh.Eksp.Teor.Fiz. 5 (5 May 1967), 1967, URL: https://doi.org/10.1070/PU1991v034n05ABEH002497.

[4] Makoto Kobayashi and Toshihide Maskawa
"CP-Violation in the Renormalizable Theory of Weak Interaction"
Progress of Theoretical Physics 49 (2 Feb. 1973), 1973, URL: https://dx.doi.org/10.1143/PTP.49.652.

[5] S. Navas et al. (Particle Data Group)
"Review of Particle Physics"
Physical Review D 110 (3 Aug. 2024), 2024, URL: https://journals.aps.org/prd/abstract/10.1103/PhysRevD.110.030001.

[6] Andrea Alberti et al.
"Precision determination of the Cabibbo-Kobayashi-Maskawa element Vcb"
Physical Review Letters 114 (6 Feb. 2015), 2015, URL: https://journals.aps.org/prl/abstract/10.1103/PhysRevLett.114.061802.

[7] Marzia Bordone, Bernat Capdevila, and Paolo Gambino
"Three loop calculations and inclusive V_{cb}"
Physics Letters B 822 (Nov. 2021), 2021, URL: http://dx.doi.org/10.1016/j.physletb.2021.136679.

[8] Matteo Fael, Thomas Mannel, and K. Keri Vos
"V_{cb} determination from inclusive $b \to c$ decays: an alternative method"
Journal of High Energy Physics 2019 (2 Dec. 2018), 2018, URL: http://arxiv.org/abs/1812.07472.

[9] Florian Bernlochner et al.
"First extraction of inclusive V_{cb} from q^2 moments"
Journal of High Energy Physics 2022 (10 Oct. 2022), 2022, URL: https://link.springer.com/article/10.1007/JHEP10(2022)068.

[10] G. Finauri and P. Gambino
"The q^2 moments in inclusive semileptonic B decays"
Journal of High Energy Physics 2024 (2 Feb. 2024), 2024, URL: https://link.springer.com/article/10.1007/JHEP02(2024)206.

[11] I Adachi et al.
"Determination of $|V_{cb}|$ using $\overline{B}^0 \to D^{*+} l^- \overline{\nu}_l$ decays with Belle II"
Physical Review D 108 (9 Nov. 2023), 2023, URL: http://dx.doi.org/10.1103/PhysRevD.108.092013.

[12] M. T. Prim et al.
"Measurement of differential distributions of $B \to D^* l \overline{\nu}_l$ and Implications on $|V_{cb}|$"
Physical Review D 108 (1 July 2023), 2023, URL: http://dx.doi.org/10.1103/PhysRevD.108.012002.

[13] Y Aoki et al.
"$B \to D^* l \nu_l$ semileptonic form factors from lattice QCD with Möbius domain-wall quarks"
Physical Review D 109 (7 Apr. 2024), 2024, URL: http://dx.doi.org/10.1103/PhysRevD.109.074503.

[14] G Martinelli, S Simula, and L Vittorio
"Updates on the determination of $V_{cb}, R(D^*) and |V_{ub}\ /|V_{cb}|$"
The European Physical Journal C 84 (4 2024), 2024, URL: https://doi.org/10.1140/epjc/s10052-024-12742-5.

[15] Paolo Gambino, Martin Jung, and Stefan Schacht
"The $V_{\{cb\}}$ puzzle: an update"
Physics Letters, Section B: Nuclear, Elementary Particle and High-Energy Physics 795 (May 2019), 2019, URL: http://arxiv.org/abs/1905.08209.

[16] Mark Thomson
Modern Particle Physics
Cambridge University Press, 2013, ISBN: 9781139525367.

[17] Mark Srednicki
Quantum Field Theory
Cambridge University Press, 2007, ISBN: 9780511813917.

[18] I. Bigi, M. Shifman, and N. Uraltsev
"Aspects of heavy-quark theory"
Annual Review of Nuclear and Particle Science 47 (1 Dec. 1997), 1997, URL: https://doi.org/10.1146/annurev.nucl.47.1.591.

[19] Aneesh V. Manohar and Mark B. Wise
Heavy Quark Physics
Cambridge University Press, 2000, ISBN: 9780521642415.

[20] Sheldon L. Glashow
"Partial-symmetries of weak interactions"
Nuclear Physics 22 (4 Feb. 1961), 1961, URL: https://www.sciencedirect.com/science/article/pii/0029558261904692.

[21] Steven Weinberg
"A Model of Leptons"
Physical Review Letters 19 (21 Nov. 1967), 1967, URL: https://journals.aps.org/prl/abstract/10.1103/PhysRevLett.19.1264.

[22] Abdus Salam
"Weak and Electromagnetic Interactions"
Conf.Proc.C 680519 (May 1968), 1968, URL: https://doi.org/10.1142/9789812795915_0034.

[23] *Standard Model of Elementary Particles*. Accessed on 12.03.2024. URL: https://upload.wikimedia.org/wikipedia/commons/0/00/Standard_Model_of_Elementary_Particles.svg.

[24] A. J. Bevan et al.
"The Physics of the B Factories"
The European Physical Journal C 2014 74:11 74 (11 Nov. 2014), 2014, URL: https://link.springer.com/article/10.1140/epjc/s10052-014-3026-9.

[25] I. I. Bigi and A. I. Sanda
CP Violation
Cambridge University Press, 2009, ISBN: 9780521847940.

[26] Kenneth G. Wilson
"Non-Lagrangian Models of Current Algebra"
Physical Review 179 (5 Mar. 1969), 1969, URL: https://journals.aps.org/pr/abstract/10.1103/PhysRev.179.1499.

[27] John C. Collins
Renormalization: An Introduction to Renormalization, the Renormalization Group and the Operator-Product Expansion
Cambridge University Press, 1984, ISBN: 9780521242615.

[28] Thomas Mannel, Winston Roberts, and Zbigniew Ryzak
"A derivation of the heavy quark effective lagrangian from QCD"
Nuclear Physics B 368 (1 Jan. 1992), 1992, URL: https://doi.org/10.1016/0550-3213(92)90204-O.

[29] Michael E Peskin and Daniel V Schroeder
An introduction to quantum field theory
WEstview, 2003, ISBN: 0201503972.

[30] D. Benson et al.
"Imprecated, yet impeccable: on the theoretical evaluation of $\Gamma(B \to Xcl\nu)$"
Nuclear Physics B 665 (Aug. 2003), 2003, URL: https://arxiv.org/abs/hep-ph/0302262.

[31] Thomas Mannel, Sascha Turczyk, and Nikolai Uraltsev
"Higher Order Power Corrections in Inclusive B Decays"
Journal of High Energy Physics 2010 (11 Sept. 2010), 2010, URL: http://arxiv.org/abs/1009.4622.

[32] I. Bigi et al.
"High power n of m_b in b-flavored widths and $n = 5 \to \infty$limit"
Physical Review D 56 (7 Oct. 1997), 1997, URL: https://journals.aps.org/prd/abstract/10.1103/PhysRevD.56.4017.

[33] G. 't Hooft
"Dimensional regularization and the renormalization group"
Nuclear Physics B 61 (C Sept. 1973), 1973, URL: https://doi.org/10.1016/0550-3213(73)90376-3.

[34] Helmut Wiedemann
Particle Accelerator Physics
Springer International Publishing, 2015, ISBN: 978-3-319-18316-9.

[35] William R. Leo
Techniques for Nuclear and Particle Physics Experiments
Springer Berlin Heidelberg, 1994, ISBN: 3540173862.

[36] Christian Lippmann
"Particle identification"
Nuclear Instruments and Methods in Physics Research Section A: Accelerators, Spectrometers, Detectors and Associated Equipment 666 (Feb. 2012), 2012, URL: http://dx.doi.org/10.1016/j.nima.2011.03.009.

[37] Kazunori Akai, Kazuro Furukawa, and Haruyo Koiso
"SuperKEKB Collider"
Nuclear Instruments and Methods in Physics Research, Section A: Accelerators, Spectrometers, Detectors and Associated Equipment 907 (Sept. 2018), 2018, URL: http://arxiv.org/abs/1809.01958.

[38] E. Kou et al.
"The Belle II Physics Book"
Progress of Theoretical and Experimental Physics 2019 (12 Aug. 2018), 2018, URL: http://arxiv.org/abs/1808.10567.

[39] SuperB Collaboration
"SuperB: A High-Luminosity Asymmetric e+ e- Super Flavor Factory. Conceptual Design Report"
(2007), 2007, URL: https://arxiv.org/abs/0709.0451.

[40] T. Abe et al.
"Belle II Technical Design Report"
(Nov. 2010), 2010, URL: https://arxiv.org/abs/1011.0352v1.

[41] *Belle II official Website*. Accessed on 03.04.2024. URL: https://www.belle2.org/archives.

[42] H Quinn
"The BABAR Physics Book: Physics at an Asymmetric B Factory"
(May 2010), 2010, URL: https://doi.org/10.2172/979931.

[43] J. P. Lees et al.
"Time-integrated luminosity recorded by the BABAR detector at the PEP-II e+e- collider"
Nuclear Instruments and Methods in Physics Research Section A: Accelerators, Spectrometers, Detectors and Associated Equipment 726 (Oct. 2013), 2013, URL: https://arxiv.org/abs/1301.2703.

[44] T. S. Hill
"The CLEO II silicon vertex detector"
Nuclear Instruments and Methods in Physics Research Section A: Accelerators, Spectrometers, Detectors and Associated Equipment 418 (1 Nov. 1998), 1998, URL: https://www.sciencedirect.com/science/article/pii/S0168900298007141.

[45] Karl Berkelman
A personal history of CESR and CLEO: The Cornell electron storage ring and its main particle detector facility
World Scientific Publishing Co., 2004, ISBN: 9789812567246.

[46] P. Aarnio et al.
"The DELPHI detector at LEP"
Nuclear Instruments and Methods in Physics Research Section A: Accelerators, Spectrometers, Detectors and Associated Equipment 303 (2 June 1991), 1991, URL: https://www.sciencedirect.com/science/article/pii/016890029190793P.

[47] R Blair et al.
"The CDF II Detector Technical Design Report"
(Jan. 1996), 1996, URL: https://lss.fnal.gov/archive/design/fermilab-design-1996-01.pdf.

[48] Valerio Bertacchi et al.
"Track Finding at Belle II"
Computer Physics Communications 259 (Mar. 2020), 2020, URL: http://arxiv.org/abs/2003.12466.

[49] Rudolf Frühwirth et al.
"Track finding in silicon trackers with a small number of layers"
Nuclear Instruments and Methods in Physics Research Section A: Accelerators, Spectrometers, Detectors and Associated Equipment 732 (Dec. 2013), 2013, URL: https://www.sciencedirect.com/science/article/pii/S0168900213008607.

[50] Johannes Rauch and Tobias Schlüter
"GENFIT - a Generic Track-Fitting Toolkit"
Journal of Physics: Conference Series 608 (1 Oct. 2014), 2014, URL: http://arxiv.org/abs/1410.3698.

[51] C. Höppner et al.
"A Novel Generic Framework for Track Fitting in Complex Detector Systems"
Nuclear Instruments and Methods in Physics Research, Section A: Accelerators, Spectrometers, Detectors and Associated Equipment 620 (2-3 Nov. 2009), 2009, URL: http://arxiv.org/abs/0911.1008.

[52] R. Frühwirth
"Application of Kalman filtering to track and vertex fitting"
Nuclear Instruments and Methods in Physics Research Section A: Accelerators, Spectrometers, Detectors and Associated Equipment 262 (2-3 Dec. 1987), 1987, URL: https://www.sciencedirect.com/science/article/pii/0168900287908874.

[53] R. Frühwirth and A. Strandlie
"Track fitting with ambiguities and noise: A study of elastic tracking and nonlinear filters"

Computer Physics Communications 120 (2-3 Aug. 1999), 1999, URL: https://doi.org/10.1016/S0010-4655(99)00231-3.

[54] J. Allison et al.
"Geant4 developments and applications"
IEEE Transactions on Nuclear Science 53 (1 Feb. 2006), 2006, URL: https://doi.org/10.1109/TNS.2006.869826.

[55] S. Agostinelli et al.
"Geant4—a simulation toolkit"
Nuclear Instruments and Methods in Physics Research Section A: Accelerators, Spectrometers, Detectors and Associated Equipment 506 (3 July 2003), 2003, URL: https://doi.org/10.1016/S0168-9002(03)01368-8.

[56] S. Jadach, B. F. L. Ward, and Z. Was
"The Precision Monte Carlo Event Generator KK For Two-Fermion Final States In e+e- Collisions"
Computer Physics Communications 130 (3 Dec. 1999), 1999, URL: http://arxiv.org/abs/hep-ph/9912214.

[57] Torbjörn Sjöstrand et al.
"An Introduction to PYTHIA 8.2"
Computer Physics Communications 191 (1 Oct. 2014), 2014, URL: http://arxiv.org/abs/1410.3012.

[58] David J. Lange
"The EvtGen particle decay simulation package"
Nuclear Instruments and Methods in Physics Research Section A: Accelerators, Spectrometers, Detectors and Associated Equipment 462 (1-2 Apr. 2001), 2001, URL: https://doi.org/10.1016/S0168-9002(01)00089-4.

[59] T. Kuhr et al.
"The Belle II Core Software: Belle II Framework Software Group"
Computing and Software for Big Science 3 (1 Dec. 2019), 2019, URL: https://link.springer.com/article/10.1007/s41781-018-0017-9.

[60] F. Abudinén et al.
"Measurement of lepton mass squared moments in $B \to X_c l \overline{\nu}_l$ decays with the Belle II experiment"
Physical Review D 107 (7 Apr. 2023), 2023, URL: https://arxiv.org/abs/2205.06372.

[61] Thomas Keck et al.
"The Full Event Interpretation – An exclusive tagging algorithm for the Belle II experiment"

Computing and Software for Big Science 3 (1 July 2018), 2018, URL: http://arxiv.org/abs/1807.08680.

[62] Thomas Keck
"FastBDT: A Speed-Optimized Multivariate Classification Algorithm for the Belle II Experiment"
Computing and Software for Big Science 1 (1 Nov. 2017), 2017, URL: https://link.springer.com/article/10.1007/s41781-017-0002-8.

[63] C. Schwanda
"Moments of the Hadronic Invariant Mass Spectrum in $B \to X_c l\nu$ Decays at Belle"
Physical Review D - Particles, Fields, Gravitation and Cosmology 75 (3 Nov. 2006), 2006, URL: http://arxiv.org/abs/hep-ex/0611044.

[64] P. Urquijo
"Moments of the electron energy spectrum and partial branching fraction of $B \to X_c e\nu$ decays at Belle"
Physical Review D - Particles, Fields, Gravitation and Cosmology 75 (3 Oct. 2006), 2006, URL: http://arxiv.org/abs/hep-ex/0610012.

[65] The BABAR Collaboration and B. Aubert
"Measurement and interpretation of moments in inclusive semileptonic decays $Bbar - - > X_c l-$ nubar"
Physical Review D - Particles, Fields, Gravitation and Cosmology 81 (3 Aug. 2009), 2009, URL: http://arxiv.org/abs/0908.0415.

[66] B. Aubert
"Measurement of the Electron Energy Spectrum and its Moments in Inclusive $B \to Xenu$ Decays"
Physical Review D 69 (11 Mar. 2004), 2004, URL: http://arxiv.org/abs/hep-ex/0403030.

[67] CDF Collaboration and D. Acosta
"Measurement of the Moments of the Hadronic Invariant Mass Distribution in Semileptonic B Decays"
Physical Review D - Particles, Fields, Gravitation and Cosmology 71 (5 Feb. 2005), 2005, URL: http://arxiv.org/abs/hep-ex/0502003.

[68] S. E. Csorna and CLEO Collaboration
"Moments of the B Meson Inclusive Semileptonic Decay Rate using Neutrino Reconstruction"
Physical Review D - Particles, Fields, Gravitation and Cosmology 70 (3 Mar. 2004), 2004, URL: http://arxiv.org/abs/hep-ex/0403052.

[69] The DELPHI Collaboration and J. Abdallah
"Determination of heavy quark non-perturbative parameters from spectral moments in semileptonic B decays"
European Physical Journal C 45 (1 Oct. 2005), 2005, URL: http://arxiv.org/abs/hep-ex/0510024.

[70] Belle Collaboration
"Moments of the Hadronic Mass Spectrum in Inclusive Semileptonic B Decays at Belle"
(2004), 2004, URL: https://arxiv.org/abs/hep-ex/0408139.

[71] Andreas Hoecker and Vakhtang Kartvelishvili
"SVD approach to data unfolding"
Nuclear Instruments and Methods in Physics Research Section A: Accelerators, Spectrometers, Detectors and Associated Equipment 372 (3 Apr. 1996), 1996, URL: https://doi.org/10.1016/0168-9002(95)01478-0.

[72] Martin Gremm et al.
"Implications of the $B \to X l \overline{\nu}_l$Lepton Spectrum for Heavy Quark Physics"
Phys. Rev. Lett. 77 (1 July 1996), 1996, URL: https://link.aps.org/doi/10.1103/PhysRevLett.77.20.

[73] Adam F Falk, Michael Luke, and Martin J Savage
"Hadron spectra for semileptonic heavy quark decay"
Phys. Rev. D 53 (5 Mar. 1996), 1996, URL: https://link.aps.org/doi/10.1103/PhysRevD.53.2491.

[74] Michael Luke and Aneesh V. Manohar
"Reparameterisation Invariance Constraints on Heavy Particle Effective Field Theories"
Physics Letters B 286 (3-4 May 1992), 1992, URL: http://arxiv.org/abs/hep-ph/9205228.

[75] Nikolai Uraltsev
"Theoretical Aspects of Semileptonic B decays"
IPPP Durham (June 2003), 2003, URL: https://arxiv.org/abs/hep-ph/0306290v1.

[76] R. Van Tonder et al.
"Measurements of q^2 moments of inclusive $B \to X_c l^+ \nu_l$decays with hadronic tagging"
Physical Review D 104 (11 Dec. 2021), 2021, URL: https://arxiv.org/abs/2109.01685.

[77] Paolo Gambino
"B semileptonic moments at NNLO"
Journal of High Energy Physics 2011 (9 July 2011), 2011, URL: http://arxiv.org/abs/1107.3100.

[78] Paolo Gambino and Christoph Schwanda
"Inclusive semileptonic fits, heavy quark masses, and v c b"
Physical Review D - Particles, Fields, Gravitation and Cosmology 89 (1 Jan. 2014), 2014, URL: https://journals.aps.org/prd/abstract/10.1103/PhysRevD.89.014022.

[79] Y. Aoki et al.
"FLAG Review 2021"
European Physical Journal C 82 (10 Nov. 2021), 2021, URL: http://arxiv.org/abs/2111.09849.

[80] Matteo Fael, Kay Schönwald, and Matthias Steinhauser
"On the relation between the $\overline{MS}$ and the kinetic mass of heavy quarks"
Physical Review D 103 (1 Nov. 2020), 2020, URL: http://arxiv.org/abs/2011.11655.

[81] Matteo Fael, Kay Schönwald, and Matthias Steinhauser
"The Kinetic Heavy Quark Mass to Three Loops"
Physical Review Letters 125 (5 May 2020), 2020, URL: http://arxiv.org/abs/2005.06487.

[82] Florian Herren and Matthias Steinhauser
"Version 3 of RunDec and CRunDec"
Computer Physics Communications 224 (Mar. 2017), 2017, URL: http://arxiv.org/abs/1703.03751.

[83] Nikolai Uraltsev
"On the chromomagnetic expectation value μ_G^2 and higher power corrections in heavy flavor mesons"
Physics Letters, Section B: Nuclear, Elementary Particle and High-Energy Physics 545 (3-4 Nov. 2001), 2001, URL: http://arxiv.org/abs/hep-ph/0111166.

[84] Paolo Gambino and Nikolai Uraltsev
"Moments of semileptonic B decay distributions in the $1/m_b$ expansion"
European Physical Journal C 34 (2 Jan. 2004), 2004, URL: http://arxiv.org/abs/hep-ph/0401063.

[85] Hans Dembinski et al. *scikit-hep/iminuit*. Oct. 2024. DOI: 10.5281/zenodo.13923658. URL: https://doi.org/10.5281/zenodo.13923658.

[86] F. James and M. Roos
"Minuit - a system for function minimization and analysis of the parameter errors and correlations"
Computer Physics Communications 10 (6 Dec. 1975), 1975, URL: https://doi.org/10.1016/0010-4655(75)90039-9.

[87] Dante Bigi et al.
"QED effects in inclusive semi-leptonic B decays"
(Sept. 2023), 2023, URL: https://arxiv.org/abs/2309.02849v2.

[88] Elisabetta Barberio, Bob van Eijk, and Zbigniew Was
"Photos — a universal Monte Carlo for QED radiative corrections in decays"
Computer Physics Communications 66 (1 July 1991), 1991, URL: https://doi.org/10.1016/0010-4655(91)90012-A.

[89] Matteo Fael, Kay Schönwald, and Matthias Steinhauser
"A first glance to the kinematic moments of $B \to X_c \ell \nu$ at third order"
Journal of High Energy Physics 2022 (8 May 2022), 2022, URL: http://arxiv.org/abs/2205.03410.

[90] Sascha Turczyk
"Additional Information on Heavy Quark Parameters from Charged Lepton Forward-Backward Asymmetry"
Journal of High Energy Physics 2016 (4 Feb. 2016), 2016, URL: http://arxiv.org/abs/1602.02678.

[91] Florian Herren
"The forward-backward asymmetry and differences of partial moments in inclusive semileptonic B decays"
SciPost Physics 14 (2 May 2022), 2022, URL: http://arxiv.org/abs/2205.03427.

[92] Paolo Gambino, Kristopher J. Healey, and Sascha Turczyk
"Taming the higher power corrections in semileptonic B decays"
Physics Letters, Section B: Nuclear, Elementary Particle and High-Energy Physics 763 (June 2016), 2016, URL: http://arxiv.org/abs/1606.06174.

[93] Ipsita Ray and Soumitra Nandi
"Test of new physics effects in $\overline{B} \to (D^{(*)}, \pi) l^- \overline{\nu}_l$ decays with heavy and light leptons"
Journal of High Energy Physics 2024 2024:1 2024 (1 Jan. 2024), 2024, URL: https://link.springer.com/article/10.1007/JHEP01(2024)022.

[94] Judd Harrison and Christine T.H. Davies
"$B \to D^*$ vector, axial-vector and tensor form factors for the full q^2 range from lattice QCD"
Physical Review D 109 (9 May 2024), 2024, URL: https://journals.aps.org/prd/abstract/10.1103/PhysRevD.109.094515.

[95] A Bazavov et al.
"Semileptonic form factors for $B \to D^* l \nu_l$ at nonzero recoil from 2+1-flavor lattice QCD"
The European Physical Journal C 82 (12 Dec. 2022), 2022, URL: http://dx.doi.org/10.1140/epjc/s10052-022-10984-9.

[96] Paolo Gambino et al.
"Inclusive semileptonic B-decays from lattice QCD"
(Nov. 2022), 2022, URL: https://arxiv.org/abs/2211.11833v1.

[97] P. Gambino et al.
"On the study of inclusive semileptonic decays of B_s-meson from lattice QCD"
Nuovo Cimento della Societa Italiana di Fisica C 47 (3 Nov. 2023), 2023, URL: https://arxiv.org/abs/2311.09892v2.